Instrument Science Report WFC3 2016-03

UVIS 2.0 Chip-dependent Inverse Sensitivity Values

S.E. Deustua, J. Mack, A.S. Bowers, S. Baggett, V. Bajaj, T. Dahlen, M. Durbin, C. Gosmeyer, H. Gunning, D. Hammer, G. Hartig, H. Khandrika J. MacKenty, R. Ryan, E. Sabbi, M. Sosey
8 November 2016

ABSTRACT

We analyze 6 years of standard star observations acquired with the WFC3/UVIS imager between 2009 and 2015. Observations of the three white dwarf standard stars, GD 153, GD 71, and G191B2B were obtained at multiple dither positions near the center of the array and in all four-corner subarrays. Departing from previous practice, chip-dependent inverse sensitivities are computed at r=10 pixels (0.3962 arcsec) for the 42 full frame filters (excluding the 20 quad filters); and these data also provide encircled energy fractions as a function of filter. Chip-dependent inverse sensitivities differ on average by 3% from previous computations, primarily due to drizzling errors. UVIS2 science data are scaled to UVIS1 by the inverse sensitivity ratio so that only a single photflam value is needed for the full detector. We describe the UVIS 2.0 (chip-dependent) philosophy and discuss our results in the context of prior photometric calculations. An updated version of CALWF3 (version 3.3) is required to process the new chip-dependent solutions.

1. Introduction

The Wide Field Camera 3 (WFC3) UVIS imaging channel consists of two e2v CCDs mounted and packaged side by side. The CCDs are butted with a separation of ~ 31 pixels. Additional optical elements include 62 filters plus one grism, altogether spanning the wavelength range between 200 to 1100 nm. Details of the WFC3 UVIS instrument and its operation are available in the WFC3 Instrument Handbook (IHB, Dressel 2016), as well as in Instrument Science Reports (ISRs) and Technical Instrument Reports (TIRs are available upon request).

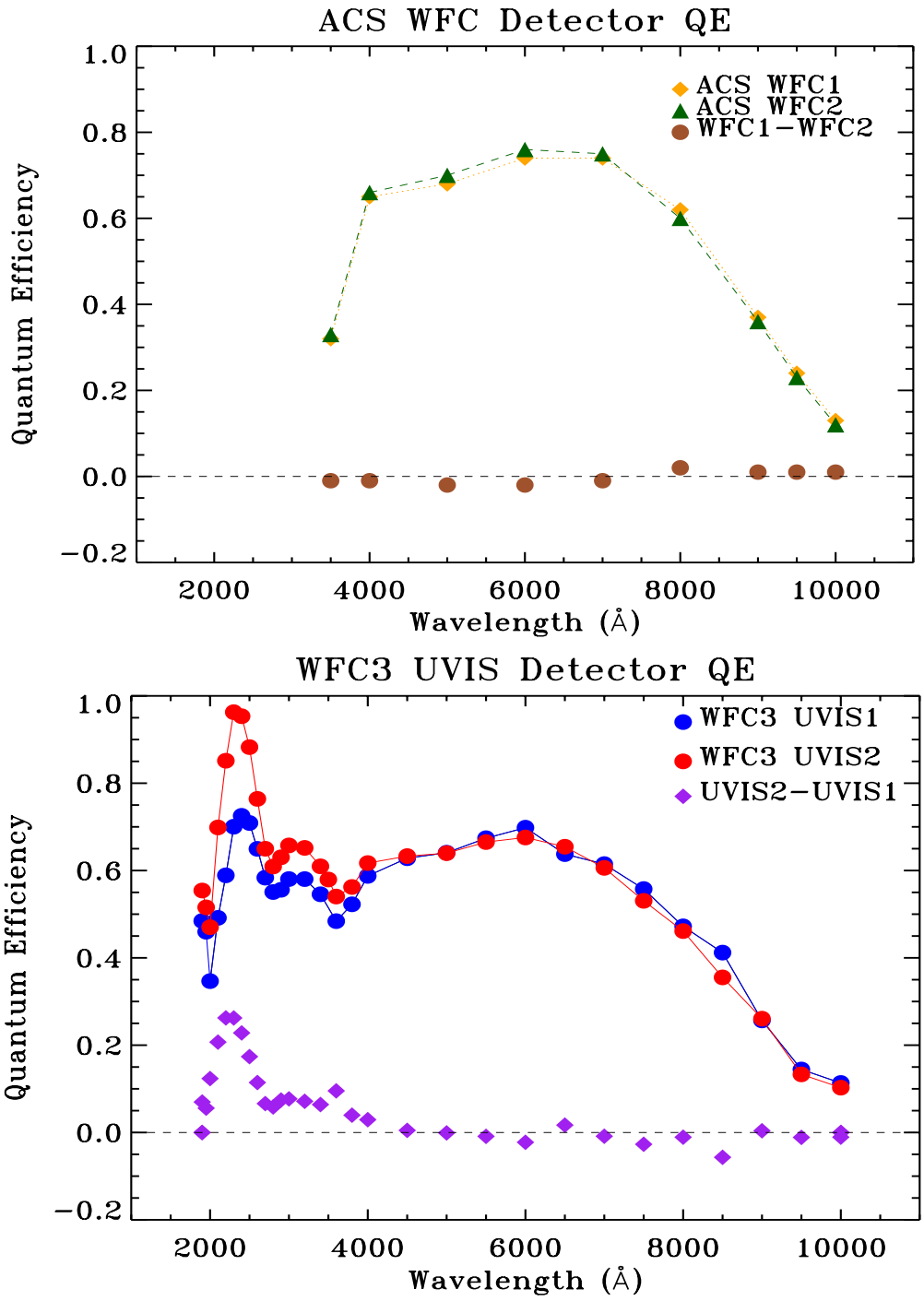

Figure 1 Top Panel: Measured quantum efficiencies for the two ACS WFC detectors (solid diamonds and triangles), and their difference, WFC1-WFC2 (orange circles). Bottom Panel: Quantum efficiency for WFC3, as measured during the 2008 ground tests (TV3), for UVIS1 (blue circles), UVIS2 (red circles), and their difference, UVIS2-UVIS1 (purple diamonds). UVIS2 is almost 30% more sensitive in the UV than UVIS1, but both WFC3 CCDs have similar QE at wavelengths $\lambda > 4500$ Å

When WFC3 was first placed in the Hubble Space Telescope during the 2009 Servicing Mission, the data reduction pipeline treated the array as a single detector with respect to photometric reduction, as was done for the Advanced Camera for Surveys (ACS) Wide Field Camera (WFC), which has two CCDs. The ACS/WFC flatfield is continuous across the two ACS CCDs, and only one value for the inverse sensitivity per filter is computed. This approach works well for ACS/WFC, because both of its CCDs were selected to have similar properties, including quantum efficiency (top panel of Figure 1) (Clampin et al. 1998).

However, motivated by the different quantum efficiency of each of the WFC3/UVIS e2v detectors (bottom panel of Figure 1) and other differences between the WFC3 chips, such as thickness, as well as the desire to improve both the accuracy and the precision of WFC3 UVIS photometry we opted to change how the WFC3 UVIS photometric calibration is determined. The "Two Chip Solution" (also referred to as UVIS 2.0) calculates chip-dependent flatfields and photometry for each filter plus CCD combination.

Changing how the WFC3/UVIS photometric calibration is implemented is not a large departure from standard practice as one might think. Earlier generation HST instruments treated each detector individually. WF/PC, a first generation HST instrument, had 8 TI CCDs: 4 for the low resolution Wide Field Camera and 4 for the high resolution Planetary Camera (Griffith 1992) plus 42 filter elements, 3 polarizers and 3 gratings. Each CCD+filter had its own photometric calibration. In 1993, WFPC2 with its four Loral CCDs plus 42 filter elements replaced WF/PC; and individual WFPC2 inverse sensitivities for each CCD+filter were computed (Holtzman et al. 1995, WFPC2 DHB). The WF/PC and WFPC2 image processing pipelines provide chip-dependent inverse sensitivity values in the calibrated image header. Thus, it is the ACS/WFC approach that is the exception.

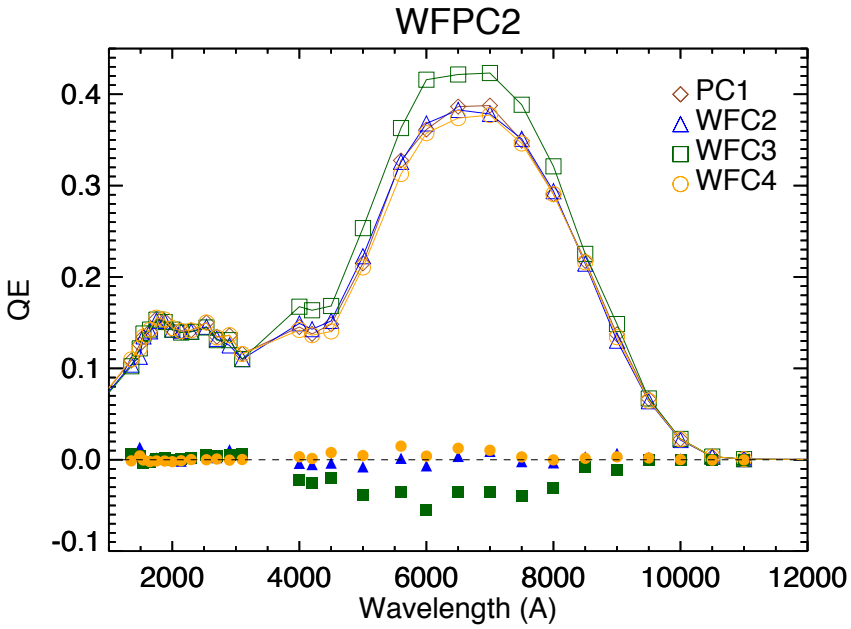

Figure 2. The pre-flight, measured quantum efficiency for each of the four WFPC2 CCDs (open symbols). The solid symbols are the QE difference between the PC1 QE and the WFC2, WFC3, and WFC4 QE (circle, square and circle, respectively).

In this ISR, we report on the new inverse sensitivities calculated for the 42 full frame filters with the new chip-dependent flatfields, and, a new photometry reference file (IMPHTTAB). The affected filters are: F200LP, F218W, F225W, F275W, F280N, F300X, F336W, F343N, F350LP, F373N, F390M, F395N, F410M, F425W, F467M, F469N, F475W, F475X, F487N, F502N, F547M, F555W, F606W, F600LP, F621M, F625W, F631N, F645N, F656N, F657N, F658N, F665N, F673N, F680N, F689M, F763M, F775W, F814W, F845M, F953N. Additionally, the SYNPHOT throughput, encircled energy, and gain tables are updated.

Appendix A contains tables of inverse sensitivities and EE fractions, as well as examples for how to use the data. Appendix B provides measured count rates at several apertures for 3 image files and Appendix C briefly describes how to recalibrate data with calwf3, version 3.3.

2. WFC3 UVIS Detector Properties

The 4096 x 2048 pixel, WFC3/UVIS CCDs were manufactured by e2v technologies; each pixel is square, 0.15 x 0.15 microns, with an average plate scale of 0.04 arcsec/pixel. The CCDs are diced from wafers processed in different foundry runs, and then placed into one package. Hence, differences in the detector properties are expected. In contrast, the ACS/WFC SiTe CCDs were diced from the same wafer and underwent similar processing (Sirianni and Clampin 2000); the resulting flat fields are continuous across the chip gap. Because the throughputs for WFC1 and WFC2 are so similar, one throughput curve is used for the two ACS CCDs. In contrast, WFC3's UVIS1 detector is almost 30% less sensitive than UVIS2 in the UV, though comparable at wavelengths $\lambda > 4500$ Å, as shown in Figure 1.

Other differences in the CCD characteristics are thickness and the imprinted patterns on the detectors. From the observed fringing pattern in the narrow band filters combined with fringing models, Wong et al. (2010) and Malamuth et al. (2003) showed that there is a significantly

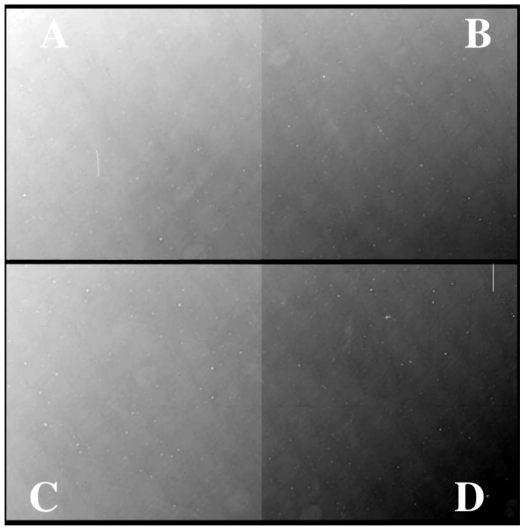

Figure 3. Cross hatch pattern seen in tungsten flat field in F390W. Image is shown in an inverted gray scale with stretch (+/-30%). Quadrants are labeled A, B (UVIS1), C, D (UVIS2). Reproduced from Figure 2 in Baggett et al. 2007.

thinner region on UVIS2. Tungsten lamp images in the UV, e.g. F390W, reveal crosshatch patterns from the CCD substrate, as can be seen in Figure 2 below, from Baggett 2007.

3. Flat Fields

New chip-dependent flat fields were created using the same data and methodology as described in Mack et al. (2013). Flats are made using the TV3 ground flats and corrected for a large internal flare and for low-frequency differences in the inflight response, as derived from dithered observations of stars in the Omega Centauri cluster. The three key differences with respect to the prior set of reference files are:

1) The star cluster observations are corrected for CTE (Charge Transfer Efficiency) effects before computing the L-flat,

2) The L-flat solutions are computed from photometry of stars on a single chip only (i.e. they exclude stars dithered from one chip to the other), and

3) The flats are independently normalized using the median value for each chip, rather than to a small region on amplifier A, which changed the normalization by less than 1% for filters with pivot wavelengths longer than 4000 Å.

UV flats are based on ground test data obtained in ambient conditions, and have been corrected for the ~3% sensitivity variations due to the crosshatch pattern (on scales of 50-100 pixels) on both chips. A complete description of these new, chip-dependent flat fields are in Mack et al. (2016).

4. Standard Star Data

Standard star data have been obtained every year since WFC3's installation in HST in 2009. All of the WFC3 photometric calibration programs observe one or more of the 3 primary HST standard stars: the white dwarfs GD153, GD71 and G191B2B. Additional monitoring programs acquire imaging data for the G-type star P330E and the white dwarf star GRW+70 5824. However, GRW+70 5824 has a poor CALPSEC[1] spectral energy distribution (SED) and is not considered a reliable flux standard. Exposure times are chosen to provide very high signal to noise ratios, S/N = 100-1000, within the standard aperture with radius r=10 pixels (nominally 0.3962 arcsec in DRZ images). Exposure times are between 0.5 and 60 seconds; less for the broad band filters, more for the narrow band filters.

Data used in this analysis were obtained from SMOV/Cycle 17 through Cycle 22 (2009 – 2015), and consist of over 2,200 individual standard star images. Observations taken after Cycle 20 (2011) have 12 electrons post-flash to mitigate CTE losses, even though CTE effects are minimal (far less than the Poisson noise) for these bright calibration stars. Any of a 2-point dither pattern, a box dither pattern, or a combination of box and line dithers is used to mitigate detector defects and cosmic rays. Dither steps are in non-integer pixels so that the star is not centered within a pixel for at least one position, which helps to sample the PSF (point spread function).

[1] CALSPEC is the calibration database that contains the composite stellar spectra that are flux standards on the HST system at http://www.stsci.edu/hst/observatory/crds/calspec.html

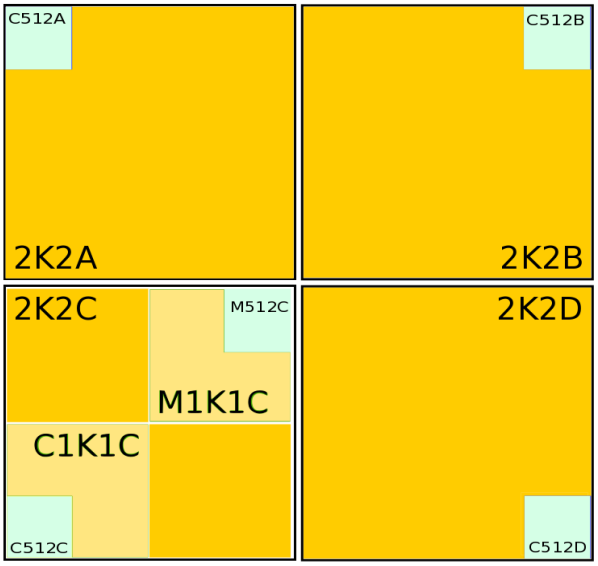

Figure 4. The four quadrants of the UVIS CCD array. Chip 1 (Amp A and B, UVIS1) is on the top, chip 2 (Amp C and D, UVIS2) on the bottom. The four corner 512 x 512 pixels subarrays and the middle 512x512 pixel subarray are the light blue squares. The chip gap is ~31 pixels and is not to scale in this figure.

Detector position diversity

Observations are obtained using standard 512 x 512 pixel subarrays at each of the four array corners, corresponding to the apertures UVIS1-C512A-SUB, UVIS1-C512B-SUB, UVIS2-C512C-SUB and UVIS2-C512D-SUB, each subtends an area on the sky of ~ 412 arcsec^2. Additional data are acquired with the standard UVIS2-M512C–SUB subarray near the middle of the UVIS detector array. These subarrays are pictured in Figure 4 where UVIS1 (chip 1) is on the top, UVIS2 (chip 2) is on the bottom. A and B amplifiers are on UVIS1 (upper left and upper right quadrants) and C and D amplifiers are on UVIS2 (lower left and lower right quadrants).

Imaging data for the 3 white dwarfs were acquired with the C512A and C512B subarrays on UVIS1, and the C512C, M512C and C512D subarrays on UVIS2, as listed in Table 1. Beginning in 2012 with Cycle 20, white dwarf observations are acquired on two corner subarrays each cycle, A and D or B and C, with each pair alternating every year. This strategy allows for yearly observations on both CCDs while mitigating CTE effects and minimizing the number of calibration orbits. A separate set of programs, 12090, 12707, 13096 and 13584, stepped a standard star over the entire UVIS focal plane array using custom 512x512 subarrays and measured the photometric repeatability for filters with pivot wavelength $\lambda > 3000$ Å to be better than 0.7% (rms), and for the UV filters to be 1.8% (rms) (Mack, Rajan & Bowers, 2015). Table 1 summarizes the subarrays, filters and standard star observations obtained between 2009 and 2015.

Table 1. Proposal IDs, filters and subarrays for the star observations used in this analysis

Program	Star	Subarray: Filters
11450 SMOV 2009	GD153	**C512A:** F218W, F225W, F275W, F280N, F300X, F336W, F343N, F350LP, F373N, F390M, F390W, F395N, F410M, F438W, F467M, F469N, F475W, F475X, F487N, F502N, F547M, F555W, F600LP, F606W, F621M, F625W, F645N, F656N, F658N, F665N, F673N, F689M, F763M, F775W, F814W, F845M, F953N
11903 Cycle 17 2009-2010	G191B2B	**C512A & C512C:** F200LP, F218W, F225W, F275W, F280N, F300X, F336W, F343N, F350LP, F373N, F390M, F390W, F395N, F410M, F438W, F467M, F469N, F475W, F475X, F487N, F502N, F547M, F555W, F600LP, F606W, F621M, F625W, F631N, F645N, F656N, F657N, F658N, F665N, F673N, F680N, F689M, F763M, F775W, F814W, F845M, F850LP, F953N
	GD153	**C512A:** F225W, F275W, F336W, F350LP, F390W, F438W, F467M, F469N, F475W, F502N, F547M, F555W, F606W, F814W, F850LP **C512C:** F467M, F469N, F502N, F547M, F606W, F814W
	GD71	**C512A:** F225W, F275W, F336W, F350LP, F390W, F438W, F555W, F775W, F850LP **C512C:** F606W, F814W, F467M, F547M, F469N, F502N
12334 Cycle 18 2010-2011	G191B2B	**M512C**: F225W, F275W, F336W, F390W, F438W, F475W, F555W, F606W, F814W
	GD153	**M512C:** F225W, F275W, F336W, F390W, F438W, F475W, F555W, F606W, F814W, F850LP
	GD71	**M512C:** F225W, F275W, F336W, F390W, F438W, F475W, F555W, F606W, F814W
12699 Cycle 19 2011-2012	GD153	**M512C**: F225W, F275W, F336W, F390W, F438W, F475W, F555W, F606W, F814W, F850LP
	GD71	**M512C:** F225W, F275W, F336W, F390W, F438W, F475W, F555W, F606W, F814W
13089 Cycle 20 2012-2013	GD153	**C512A & C152D:** F200LP, F218W, F225W, F275W, F280N, F300X, F336W, F343N, F350LP, F373N, F390M, F390W, F395N, F410M, F438W, F467M, F469N, F475W, F475X, F487N, F502N, F547M, F555W, F600LP, F606W, F621M, F625W, F631N, F645N, F656N, F657N, F658N, F665N, F673N, F680N, F689M, F763M, F775W, F814W, F845M, F850LP, F953N
13575 Cycle 21 2013-2014	GD153	**C512B & C512C:** F200LP, F218W, F225W, F275W, F280N, F300X, F336W, F343N, F350LP, F373N, F390M, F390W, F395N, F410M, F438W, F467M, F469N, F475W, F475X, F487N, F502N, F547M, F555W, F600LP, F606W, F621M, F625W, F631N, F645N, F656N, F657N, F658N, F665N, F673N, F680N, F689M, F763M, F775W, F814W, F845M, F850LP, F953N
14018 Cycle 22 2014-2015	G191B2B	**C512A & C512C:** F200LP, F218W, F225W, F275W, F300X, F336W, F350LP, F390M, F390W, F410M, F438W, F467M, F475W, F475X, F547M, F555W, F600LP, F606W, F621M, F625W, F689M, F763M, F775W, F814W, F845M, F850LP
14021 Cycle 22 2014-2015	G191B2B	**C512A**: F218W, F225W, F275W, F336W, F438W, F475W, F547M, F555W, F600LP, F606W, F621M, F625W, F775W, F814W, F845M
	GD153	**C512A & C512C:** F218W, F225W, F275W, F336W, F350LP, F438W, F475W, F547M, F555W, F600LP, F606W, F621M, F625W, F775W, F814W, F845M

Image Processing

All observations of the white dwarf stars, GD71, GD153, and G191B2B, spanning the time period from July 2009 to July 2015 are processed using *calwf3 version 3.3* with the new chip-dependent flatfields (Mack et al. 2016) and with the most recent reference files for distortion and gain corrections, and bias and dark subtractions. Observations are also corrected for charge transfer inefficiency (i.e. CTE-corrected).

AstroDrizzle is used to combine observations of each star over the full 6-year time period in order to maximize the signal-to-noise of the derived photometry. First, drizzled products for each filter are created using observations obtained in the same visit using the same subarray position and exposure time. Cosmic-ray flags are derived using these visit-level products rather than the combined dataset in order to limit flagging of PSF optical structure. For example, the UVIS PSF exhibits large spatial variations across the detector, especially in the C512A subarray, which is nominally out of focus relative to the rest of the detector and is highly sensitive to breathing. On one side of focus, the PSF is elongated along the 45 degree diagonal and on the other side of focus along the 135 degree diagonal (Anderson et al. 2015). Additionally, the signal-to-noise of the complete dataset varies significantly over the 6-year period, where later observations of the same standards obtained longer exposures just below the saturation limit. These later observations have much higher signal-to-noise in the PSF wings, including in the Airy rings.

Once the visit-level flags are computed, then all the observations per filter per chip per star are combined using AstroDrizzle, taking care to retain the cosmic-ray flags determined from each visit but with no additional flagging or rejection of data to prevent loss of signal. The result is a set of clean 'master' images, in e-/sec, which are then used to obtain aperture photometry.

Simply combining all the flt files with AstroDrizzle resulted in drz photometry that was on average 3-4% fainter compared to photometry from the flt*PAM. When examining both the weight image of the 2012 drizzled products and the data quality flags in the individual calibrated images, the PSF wings between radii of 5 and 20 pixels were flagged as cosmic rays. These calibration monitoring programs obtain observations over a long time baseline at a range of

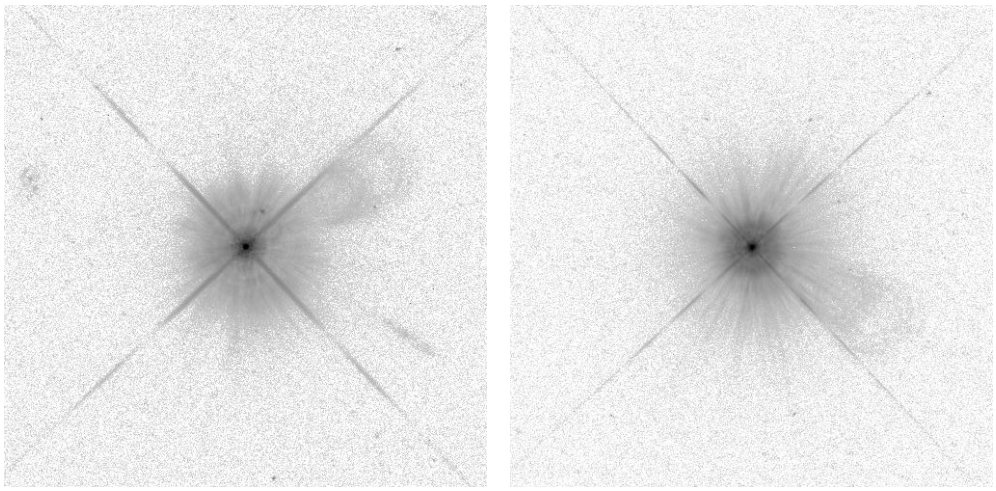

Figure 5. Deep images, uncorrected for distortion, from Program 11438 for filter F275W (right) in Amp B and F625W (left) in Amp A with a 6 dex log stretch. Each image subtends ~20 arcsec on a side, ghosts due to the detector windows are evident, as well as some field objects (Hartig 2009)

detector orientations. As a result, the PSF diffraction spikes, Airy rings, and other optical effects are fixed in detector space but change position when translated to sky coordinates by AstroDrizzle, making these features susceptible to improper flagging as cosmic rays. A good illustration of these effects is in Hartig (2009) whose figures include a color coded schematic of the EE (encircled energy fraction) with position and PSF, the PSF cores for five positions in two filters, and artifacts in the wings of the PSF in deep exposures. The latter is reproduced here as Figure 5.

Furthermore, the signal-to-noise of the complete dataset varies significantly over the 6 year period, where later observations of the same standards are obtained with longer exposures to obtain counts just below the saturation limit, and as a consequence, have much higher signal-to-noise in the diffraction spikes and PSF wings. For example, observations of GD153 in F438W consisted of approximately equal numbers of 1.0-second exposures (S/N~100) from program 11450 and 6.0-second exposures (S/N~250) from program 11903. When cosmic-ray flags are computed using input frames with very different S/N, orientations, or detector positions, AstroDrizzle's cosmic-ray rejection can flag real PSF structure. Incorrect flagging of PSF structure as cosmic-rays results in a measured signal smaller than the average of the signal obtained from individual files. The solution is to first drizzle the visit level exposures and then co-add the visit level images using AstroDrizzle without added flagging or rejection.

As an additional check of the new drizzled PSF results, we compare the measured signal in the same aperture for the drizzle-combined products to the average flux computed from undrizzled calibrated frames (corrected only for varying pixel area) and find that the flt and drz photometry agree to better than 1%. These new drizzled data products are used to compute both the UVIS chip-dependent encircled energy (Bowers, Mack & Deustua, 2016) and inverse sensitivities.

Aperture Photometry

Aperture photometry is performed on the final, co-added master images, using the PyRAF task, DAOPHOT. Sky values are determined from the mean of pixels at radius r= 152 to 197 pixels (~6 – 8 arcsecs). If the star is not centered on the subarray, the edge of the subarray may be less than 200 pixels (Bowers, Mack & Deustua, 2016). Because the rms repeatability in apertures between 10 and 30 pixels (0.3962 to 1.189 arcsec) are nearly identical, and because a 10-pixel radius is more useful for often-crowded science images, **the smaller aperture radius is the new baseline for the PHOTFLAM value that appears in science data headers.** This fundamental change from the infinite aperture photflam is flagged in the image data headers, which reference this ISR. The ratios of observed to synthetic count rate within that 10 pixel aperture for the white dwarf standards are averaged for each CCD+filter combination and are used to correct the system throughput R, and then to determine the inverse sensitivities according to Equation 4.

Encircled Energy and Aperture Corrections

Bowers et al. (2016) describe the filter-based EE measurements made from the 'master' drizzled images. EE curves from flt images are more peaked at radii less than 5 pixels compared to the EE values from drizzled images, as shown in Bowers et al's Figure 8 for F225W, F475W, F606W, and F814W. Compared to the drizzled EE values, the FLT EE fractions are ~3% higher at r=2 pixels, ~1% higher at 3 pixels, and at 5 pixels they are effectively identical. Drizzling smooths the point-spread function (PSF). Each of the filter+CCD 'master' drizzled images is

made by combining all the data, EE curves derived from the 'master' images are used to compute the new inverse sensitivities, since many users rely on drizzled data for their analyses[2]. Confidence in this approach is supported by the data from Hartig's study of the WFC3/UVIS PSF and EE curves.

Hartig measured the PSF of the bright star, GD 153, on flt images. The star was placed at 5 locations on the UVIS array, and the encircled energy fraction is determined from aperture radii between 0.1 arcsec (2.5 pixels) to 3 arcsec (75 pixels) from this very high signal to noise data. In Figure 6, the Hartig EE fraction averaged over the entire array is plotted with 3σ error bars. The standard deviation in the Hartig derived EE fractions is ~1% for r < 0.12 arcsec (3.0 pixels), and <0.1% at r > 0.5 arcsec (12.6 pixels). In the F275W filter, Amp A has the largest difference (1.4%) in EE fraction at r=0.1 arcsec relative to the mean value over the focal plane array. Amp D shows the largest difference in the F625W.

Standard star data used to determine in-flight encircled energy (EE) curves for each filter+CCD have signal to noise ratios between SN~200 and SN ~700 (depending on filter), which provide reliable measurements out to an aperture radius of r~35 pixels. The Hartig post-SMOV encircled energy model is interpolated in wavelength and EE fraction to the pivot wavelength of each filter and aperture radii. At r=35 pixels the 'two-chip' drizzled EE curves are normalized and spliced to the Hartig model.

An example of the differences between the various encircled energy values shown in Figure 7 for the F625W filter. The brown diamonds are the average Hartig 2009 data, and the green dash dotted line is the model interpolated to the F625W pivot wavelength. EE values for the WFC3/UVIS detectors were calculated from aperture photometry for radii between 2 and 151 pixels, and normalized to the encircled fraction at r= 6 arcsec (before splicing into the model),

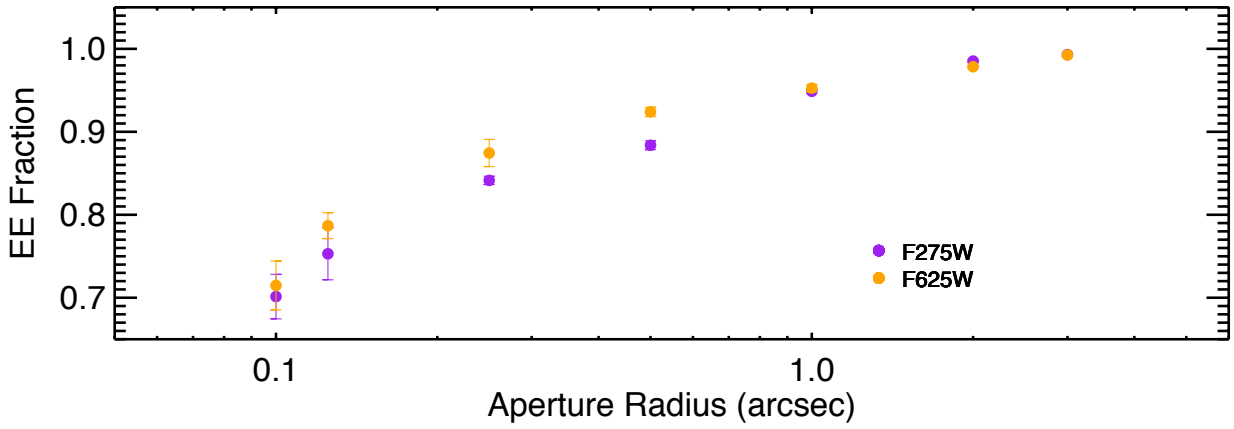

Figure 6. The average encircled energy fraction based on measurements made at 5 positions on the UVIS field of view: one at each corner subarray and one near the center of the UVIS array in two filters (Hartig 2009). Plotted are the averages and 3σ error bars for F275W (purple circles) and F625W (gold circles). At radii greater than 1″ (25 pixels) the standard deviation is less than 0.001.

[2] As the AstroDrizzle configuration files in the pipeline are not optimized for all types of observations, the pipeline drizzled images (drz files) are often erroneous, i.e. flux in the drz differs from flux in the flt files. We recommend users check their drz files, and re-drizzle if necessary, changing drizzle parameters as needed.

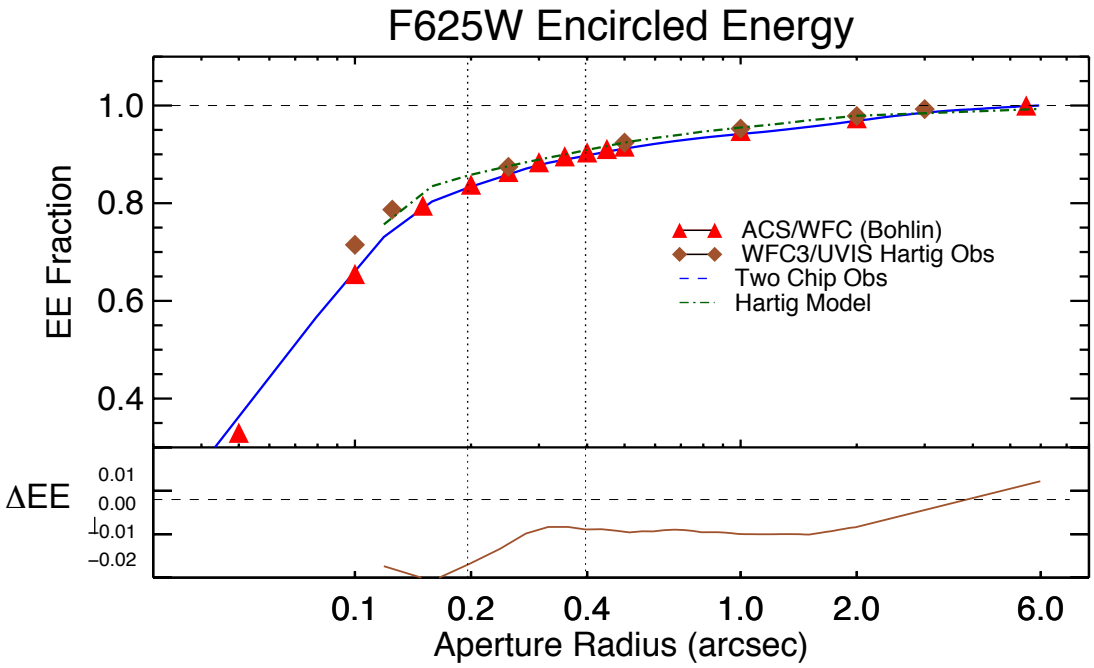

Figure 7. Top: Measured encircled energy values for the F625W bandpass from ACS/WFC (solid red triangles Bohlin 2016), from WFC3/UVIS Two Chip (dashed line) and Hartig's SMOV programs (solid brown diamonds). The dash dotted line is the EE for F625W interpolated from the Hartig model (Hartig 2009). All WFC3/UVIS values are averages over the detector. WFC3/UVIS Two Chip EE fractions are normalized to 0.995 at 6 arcsec (152 pixels). For r < 0.4 arcsec, the two chip EE fractions are in closer agreement with the ACS/WFC values compared to either of the Hartig observed or model values. The two vertical lines mark r=0.1986 arcsec (5 pixels, left) and r=0.3962 arcsec (10 pixels, right). Bottom: Difference between Two Chip observed and Hartig model (obs - model).

e.g. as in Table 19 for F275W and F625W. The average EE fraction at 6 arcsec is ~0.995, within an accuracy of 0.5% (Hartig, private communication). The EE values of the two CCDs are virtually identical; the blue dashed line represents their average. For comparison, the measured encircled energy values for the ACS/WFC F625W bandpass are also plotted with solid red triangles (Bohlin 2016), with which the WFC3 two-chip EE values (blue solid line) are in excellent agreement. Hartig's observations are shown as solid brown diamonds. WFC3/UVIS values are averages over the two CCDs. WFC3/UVIS Two Chip EE fractions are normalized by the encircled signal at 6 arcsec (~151 pixels). For r < 0.4 arcsec, the two chip EE fractions are in closer agreement with the ACS/WFC values compared to either of the Hartig observed or model values.

While users are advised to measure aperture corrections directly from their observations to account for variations in focus, these tabulated EE fractions may be used when that approach is not possible. The EE fraction is constant for large apertures (r ≥10 pixels) but the variation in measured photometry at r= 3 pixels relative to photometry at r=10 pixels can be as large as 10% (cf. Sabbi & Bellini 2011) unless 'breathing' and focus effects are accounted for.

The in-flight, filter based encircled energy values, i.e. aperture corrections, are provided for the WFC3/UVIS detectors in Tables 12-16 in Appendix A. The files, wfc3uvis1_aper_005_syn.fits and wfc3uvis2_aper_005_syn.fits are available from the CRDS (Calibration Reference Data

System).[3] For convenience, Hartig's model values are reproduced in Table 17 these values are averages over the entire array.

UVIS Gain Values

Since WFC3's installation in HST the UVIS gain values for each quadrant have remained constant to within 1% (Martlin and Gunning 2016). The synphot gain file is updated to these values from the pre-launch, nominal 1.5 electrons/DN. The average UVIS gain between 2009 and 2015 is 1.559, 1.554, 1.578, 1.559 e-/DN for amps A, B, C, D; the standard deviation is 0.0094, 0.0067, 0.0085, 0.0072. The new gain file (wfc3_uvis_dn_002_syn.fits) is available from CRDS.

5. Computing the New Inverse Sensitivity Values

Calculating the Inverse Sensitivities

Following the Bohlin (2014) methodology, the photon weighted mean flux within a bandpass is

$$\langle F \rangle = \frac{\int F_\lambda \, \lambda \, R \, d\lambda}{\int \lambda \, R \, d\lambda} = SN_e \qquad \text{Equation 1}$$

where F_λ is the source spectral flux density in ergs s^{-1} cm^{-2} $Å^{-1}$, R is the system throughput response as a function of wavelength, S is the instrumental calibration constant called inverse sensitivity (PHOTFLAM) and N_e is the measured instrumental count rate in electrons s^{-1} in an infinite aperture. If the instrument throughput parameters and source flux density is known, the count rate can be predicted from:

$$N_e = \frac{A}{hc} \int F_\lambda \, \lambda \, R \, d\lambda \qquad \text{Equation 2}$$

where A is the telescope area, h is Planck's constant and c is the speed of light, rewriting equation 1:

$$S = \frac{\langle F \rangle}{N_e} = \frac{hc}{A \int \lambda \, R \, d\lambda} \qquad \text{Equation 3}$$

which becomes, in the HST nomenclature,

$$photflam = \frac{flam}{N_e} \qquad \text{Equation 4}$$

In the ideal case, the instrument response would be known precisely from end-to-end measurements. In practice however, laboratory measurements are made component by component and the system throughput computed from the individual values. Often the initial total system throughput estimated this way is inaccurate, and of course, once in operation, the system throughput itself can change. Therefore, the general procedure to determine the inverse sensitivity is to apply correction factors to the synthetic photometry until the calculated count rates are equal to the observed values.

[3] Calibration Reference Data System, http://www.stsci.edu/hst/observatory/crds

New inverse sensitivity values for each CCD and filter combination are determined for a circular aperture with radius r=10 pixels, corresponding to r=0.3962 arcsec in the 'native' resolution of the UVIS channel. We use the model spectra for GD71, GD153 and G191B2B from CALSPEC: gd71_mod_010.fits, gd153_mod_010.fits and g191b2b_mod_010.fits, respectively. These models are calculated with the Rauch et al. (2013) NLTE stellar atmosphere code and include line blanketing for G191B2B. The 2012 sensitivity values were determined using CALSPEC models calculated from the Hubeny NLTE atmosphere code (see the CALSPEC webpage at http://www.stsci.edu/hst/observatory/crds/calspec.html and Bohlin et al. (2014) for further information and references).

Because the chip-dependent photometry departs from the approach implemented at the time WFC3 was installed in 2009, changes to the synthetic photometry are required. All correction factor files are removed: modified filter transmissions, (wfc3_uvis_fnnnn_xxx_syn.fits), flat field 'fudge' corrections (wfc3_uvis_fnnnnf1_xxx_syn.fits, wfc3_uvis_fnnnnf2_xxx_syn.fits), and wavelength-dependent corrections (wfc3_uvis_cor_xxx_syn.fits), effectively reverting to the pre-launch values. However, the encircled energy fractions (aperture corrections) are updated with their in-flight measured values. Table 2 lists the components and their provenance. Details of the updated synphot/pysynphot files are described in Deustua (2016).

The STSDAS synthetic photometry package, SYNPHOT, was used to determine the initial WFC3 optical throughput from the current telescope component files, pre-launch filter transmission files, and updated aperture corrections. SYNPHOT simulates photometric data and spectra as observed with the Hubble Space Telescope (HST). When the initial throughput is multiplied by the CALSPEC stellar models and by the updated aperture correction, Equation 2 and the EE for 10 pixels gives the expected count rates within an aperture of r=10 pixels for each star+filter+CCD combination. The ACS flux calibration IDL code (originally written by Bohlin) was adapted for WFC3/UVIS and utilized to compute the throughput corrections.

New inverse sensitivity values are calculated using the standard method as is done for ACS and the 2012 WFC3/UVIS solutions. First, synthetic photometry count rates for an aperture with

Table 2: OTA +WFC3 optical transmission files (synphot component files) used to compute the initial throughput values for UVIS1 and UVIS2

Component	Description	Pedigree
hst_ota_007_syn	HST OTA throughput	
wfc3_pom_001_syn	WFC3 pickoff mirror reflectivity	
wfc3_uvis_mir1_002_syn	Reflectivity of UVIS mirror 1	
wfc3_uvis_mir2_002_syn	Reflectivity of UVIS mirror 2	
wfc3_uvis_owin_002_syn	Transmission of UVIS outer window	Pre-launch
wfc3_uvis_iwin_002_syn	Transmission of UVIS inner window	
wfc3_uvis_ccd1_003_syn	Raw quantum efficiency for UVIS1	
wfc3_uvis_ccd2_003_syn	Raw quantum efficiency for UVIS2	
wfc3_uvis_fnnn_002_syn	Filter Transmission, vacuum wavelength	
wfc3uvis1_aper_004_syn	aperture correction for UVIS1	In-flight
wfc3uvis2_aper_004_syn	aperture correction for UVIS2	

radius = 10 pixels for each star+filter+CCD combination is calculated from the initial throughput to compute the mean observed to synthetic count rate ratio for each filter+CCD. Then a 3rd order polynomial is fit to the resulting ratios to compute the wavelength-dependent correction for each CCD (see Figure 8). For both UVIS1 and UVIS2 a 3rd order polynomial provides a good fit at both the shortest and longest wavelengths, and, from which the wavelength-dependent correction is calculated for λ=1700 – 11000 Å at intervals of $\Delta\lambda$=1 Å. Synthetic count rates are then recomputed for each star, the resulting ratios are averaged, and only then are the scalar correction factors determined for each filter+CCD. The filter transmission functions are multiplied by the new scalar factors creating new filter throughput files, and synthetic photometry is recomputed.

Plotted in Figure 8 are the UVIS1 and UVIS2 solutions where 3rd order fit is plotted with the solid black lines. Light-hued symbols are the filter-dependent residuals from the fit. Table 3 lists the 3rd order polynomial value and scalar correction factor for the two CCDs, as well as an estimate of the rms statistical uncertainty. The rms error is a conservative value, and is more an indication of the spread in the observed to synthetic photometry between the standard stars than a true error.

Once a satisfactory solution to the synthetic count rate is obtained, the next step is to calculate

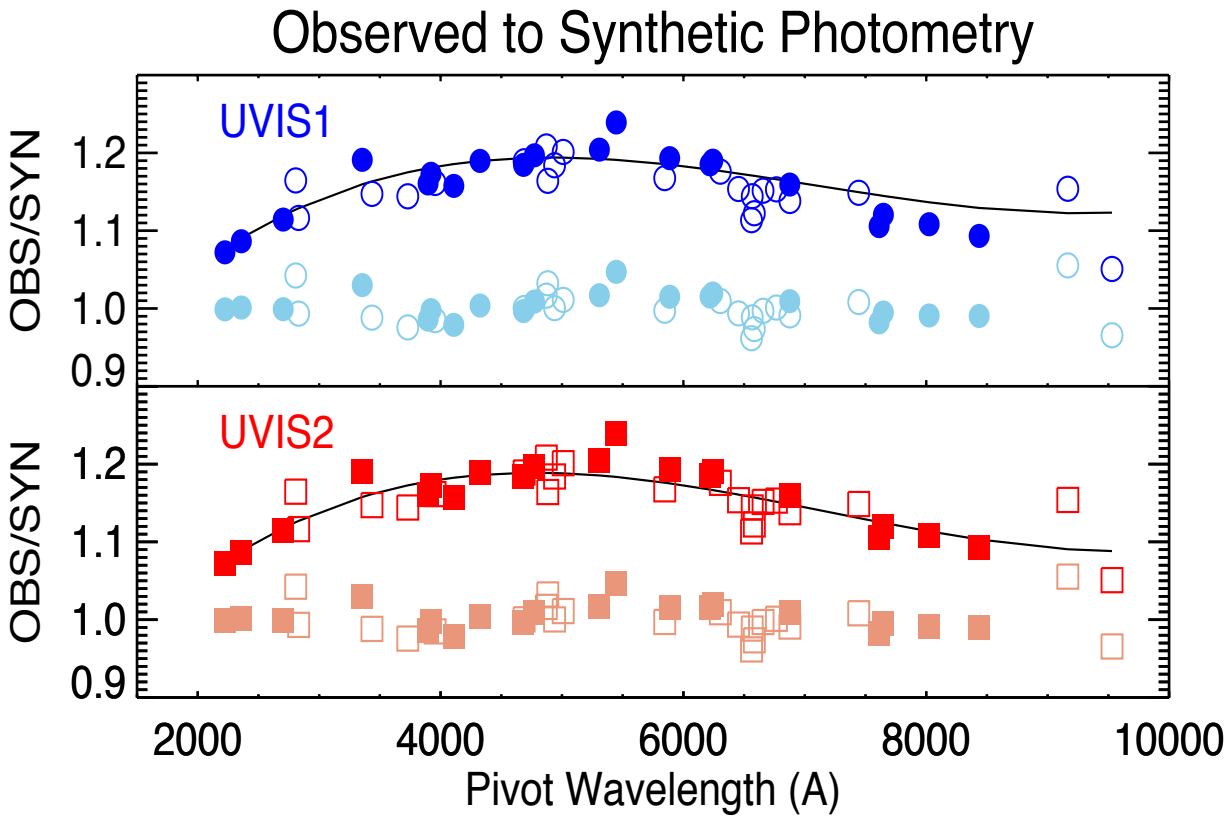

Figure 8. Polynomial fits for UVIS1 (top panel) and UVIS2 (bottom panel) plotted against filter pivot wavelength. A 3rd order polynomial is required to fit both the shortest and longest wavelengths. Solid symbols mark the broad and medium band filters, open symbols mark the narrow band, long pass and extremely wide filters. The scalar corrections to the 3rd order fit for each filter are also shown (in lighter colors) and cluster around 1. All filters were used in the fits; there is a few tenths of a percent difference in the fits with and without the narrow band filters.

the average spectral flux density, $\langle F \rangle$, (ergs-s^{-1}-cm^{-2}-$Å^{-1}$) in the filter bandpass per Equation 1 from the throughputs computed with the updated filter transmission and the stellar models. The STSDAS SYNPHOT task *calcphot* or PySynphot can be used to compute <F>, (FLAM), although we used the ACS IDL code, adapted for WFC3. Then, FLAM is divided by the observed count rate (in electrons/sec) to obtain PHOTFLAM, defined (Smith et al. 2011, Ch. 3.4) as the mean spectral flux density in ergs-s^{-1}-cm^{-2}-$Å^{-1}$ that produces 1 electron per second, and has units of ergs-cm^{-2}-$Å^{-1}$-e^{-1} in HST instrument documentation. The new inverse sensitivity values, PHTFLAM1 and PHTFLAM2 for UVIS1 and UVIS2 respectively, are listed in Tables 8 and 9 in Appendix A, along with instrumental zeropoints in the STmag, ABmag and VEGAmag photometric systems.

PHTFLAM1, PHTFLAM2 and zeropoints are provided for an aperture with radius r = 10 pixels, r = 0.3962 arcsec in the WFC3/UVIS 'natural scale' as defined by Kalirai et al (2010). ACS, for example, provides PHOTFLAM values for the infinite radius.[4] PHTFLAM1 and PHTFLAM2 for UVIS1 and UVIS2 respectively are written into image headers by the *calwf3* pipeline, described in Section 8 and in Ryan et al (2016) and Bajaj (2016).

[4] Technically, the infinite radius is defined for the aperture where 100% of the light is enclosed. In practice, this can be difficult to measure. For WFC3/UVIS, more than 99.5% of the light is enclosed within a radius of 6 arcsec and the infinite photflam is the photflam at 10 pixels divided by the encircled energy at 10 pixels.

Table 3. Values of the 3rd order polynomial fit calculated at each filter's pivot wavelength, and the filter scalar correction (columns 6 and 11) computed after applying the wavelength-dependent correction for UVIS1 (column 5) and UVIS2 (column 10). Columns 4 and 9 list the rms computed from the number of stars N (columns 2 and 7) for each filter+CCD.

	UVIS1					UVIS2				
Filter	**N**	**OBS/SYN**	**RMS**	**Poly**	**Scalar**	**N**	**OBS/SYN**	**RMS**	**Poly**	**Scalar**
F200LP	1	1.1883	-	1.1940	1.0464	1	1.1641	-	1.1886	1.0324
F218W	2	1.0793	0.0084	1.0777	1.0031	2	1.0722	0.0078	1.0754	0.9989
F225W	3	1.0910	0.0024	1.0906	1.0024	3	1.0864	0.0029	1.0885	1.0012
F275W	3	1.1227	0.0019	1.1195	1.0044	3	1.1143	0.0056	1.1177	0.9991
F280N	2	1.1125	0.0078	1.1288	0.9880	2	1.1164	0.0175	1.1270	0.9934
F300X	2	1.1545	0.0023	1.1271	1.0306	2	1.1646	0.0117	1.1253	1.0424
F336W	3	1.1935	0.0034	1.1597	1.0304	3	1.1911	0.0042	1.1577	1.0301
F343N	2	1.1438	0.0017	1.1634	0.9834	2	1.1473	0.0007	1.1614	0.9882
F350LP	3	1.1921	0.0024	1.1856	1.0117	2	1.1676	0.0076	1.1761	0.9971
F373N	2	1.1303	0.0039	1.1751	0.9619	2	1.1442	0.0030	1.1727	0.9757
F390M	2	1.1637	0.0080	1.1803	0.9860	2	1.1607	0.0153	1.1776	0.9857
F390W	3	1.1809	0.0073	1.1810	1.0021	3	1.1731	0.0030	1.1783	0.9979
F395N	2	1.1795	0.0103	1.1819	0.9980	2	1.1614	0.0067	1.1791	0.9850
F410M	2	1.1671	0.0126	1.1856	0.9844	2	1.1576	0.0131	1.1825	0.9790
F438W	3	1.1958	0.0010	1.1896	1.0059	3	1.1897	0.0036	1.1860	1.0038
F467M	2	1.1757	0.0035	1.1933	0.9853	3	1.1846	0.0003	1.1887	0.9967
F469N	2	1.1924	0.0091	1.1934	0.9992	3	1.1892	0.0015	1.1887	1.0005
F475W	3	1.2083	0.0050	1.1937	1.0143	3	1.1969	0.0039	1.1888	1.0089
F475X	2	1.1947	0.0048	1.1940	1.0049	2	1.1841	0.0122	1.1884	1.0004
F487N	2	1.2069	0.0002	1.1939	1.0109	2	1.2083	0.0003	1.1886	1.0165
F502N	2	1.2005	0.0056	1.1939	1.0056	3	1.2012	0.0011	1.1881	1.0111
F547M	2	1.2360	0.0070	1.1910	1.0380	3	1.2391	0.0014	1.1835	1.0471
F555W	3	1.2174	0.0041	1.1923	1.0224	3	1.2042	0.0040	1.1854	1.0171
F600LP	2	1.1758	0.0074	1.1495	1.0163	2	1.1487	0.0100	1.1307	1.0083
F606W	2	1.2023	0.0110	1.1849	1.0148	3	1.1932	0.0042	1.1752	1.0151
F621M	2	1.1977	0.0084	1.1785	1.0162	2	1.1853	0.0002	1.1672	1.0154
F625W	2	1.2049	0.0102	1.1781	1.0222	2	1.1900	0.0011	1.1666	1.0193
F631N	2	1.1789	0.0183	1.1768	1.0021	2	1.1759	0.0192	1.1649	1.0096
F645N	2	1.1662	0.0001	1.1734	0.9938	2	1.1536	0.0090	1.1608	0.9937
F656N	2	1.1140	0.0028	1.1710	0.9514	2	1.1135	0.0080	1.1577	0.9618
F657N	2	1.1495	0.0079	1.1709	0.9817	2	1.1443	0.0096	1.1576	0.9886
F658N	2	1.1294	0.0057	1.1705	0.9683	2	1.1224	0.0163	1.1571	0.9735
F665N	2	1.1651	0.0036	1.1688	0.9968	2	1.1514	0.0084	1.1549	0.9970
F673N	2	1.1725	0.0027	1.1661	1.0055	2	1.1531	0.0198	1.1516	1.0012
F680N	2	1.1414	0.0040	1.1634	0.9810	2	1.1382	0.0097	1.1483	0.9912
F689M	2	1.1720	0.0105	1.1635	1.0072	2	1.1593	0.0129	1.1483	1.0094
F763M	2	1.1482	0.0055	1.1456	1.0019	2	1.1059	0.0092	1.1255	0.9822
F775W	2	1.1522	0.0123	1.1447	1.0052	2	1.1204	0.0009	1.1245	0.9948
F814W	2	1.1326	0.0137	1.1365	0.9928	3	1.1083	0.0020	1.1136	0.9910
F845M	2	1.0978	0.0067	1.1292	0.9717	2	1.0933	0.0010	1.1031	0.9904
F850LP	3	1.1868	0.0052	1.1225	1.0549	2	1.1539	0.0043	1.0905	1.0554
F953N	3	1.0883	0.0010	1.1232	0.9689	3	1.0508	0.0075	1.0882	0.9656

6. Results

Synthetic Photometry

The synphot/pysynphot component and graph tables are updated to allow for chip-dependent values. The first nine files listed in Table 2 are unchanged from 2012; these are the transmission values of the HST mirrors, the pick-off mirror (which directs light into WFC3 from the telescope optical axis), and the dewar windows. The original QE values are also unchanged. Values in the synphot gain table (wfc3_uvis_dn_001_syn) were updated using the inflight determined gain values (wfc3_uvis_dn_002_syn). Although the gain is determined for each amplifier (Martlin and Gunning 2016), the average gain per chip is identical (1.55 electrons/DN) thus the synphot gain file contains only a single value for both CCDs. (The gains are applied in the flat fielding step).

Table 4. Components updated in 2016 for chip-dependent photometry

2012 Component Table	2016 Component Table	Description
wfc3_uvis_fn_004_syn or wfc3_uvis_fn_005_syn	wfc3uvis1_fn_006_syn wfc3uvis2_fn_006_syn	Pre-launch Filter Transmission multiplied by a scalar derived from 3rd order polynomial fit*
wfc3_uvis_fnf1_001_syn wfc3_uvis_fnf2_001_syn	wfc3_uvis_fnf1_003_syn wfc3_uvis_fnf2_003_syn	Midpoint of FN flat for chip 1 and chip 2. All 2016 values are set to 1
wfc3_uvis_cor_003_syn	wfc3uvis1_cor_004_syn wfc3uvis2_cor_004_syn	In-flight wavelength-dependent correction (polynomial)*
wfc3_uvis_aper_001_syn	wfc3uvis1_aper_005_syn wfc3uvis2_aper_005_syn	Aperture correction for Inflight EE fractions per filter
wfc3_uvis_dn_001_syn	wfc3_uvis_dn_002_syn	CCD gain (electron/DN) updated with inflight measured values

* This is often referred to as a detector QE correction rather than a throughput (R) correction; but these two concepts are equivalent, because the QE is a factor in the computation of R.

In the single-detector photometric calibration, 'fudge' factors, e.g. wfc3_uvis_f606wf1_001_syn and wfc3_uvis_f606wf2_001_syn, for UVIS1 and UVIS2 respectively, were employed to normalize each filter's flat field to the midpoint value for each CCD, as the flat fields were originally normalized to a small region on UVIS1. In the chip-dependent approach, this is no longer necessary, as each CCD's flat fields are independently normalized to the median of each chip. Chip dependent flat fields have smaller rms scatter than the single-detector flats (Mack, Dahlen and Bowers, 2016). The values in these 'fudge factor' files are removed and set to unity.

SYNPHOT files are created for each CCD for aperture and throughput corrections. Table 4 lists the updated 2016 component tables and compares with those used for the 2012 solutions.

The two chip-dependent aperture correction files (wfc3uvis1_aper_003_syn and wfc3uvis2_aper_003_syn) whose values are the inflight EE fractions spliced to the Hartig model as discussed above replace wfc3_uvis_aper_001_syn, the single-detector aperture correction file. Similarly, the wavelength-dependent polynomial correction tables to the transmission are now provided for each CCD (wfc3uvis1_cor_004_syn, wfc3uvis2_cor_004_syn), replacing the single-detector file, wfc3_uvis_cor_003_syn. New files were created for each CCD, which have the scalar corrected filter transmissions, wfc3uvis1_fnnnn_006_syn, wfc3uvis2_fnnnn_006_syn where fnnnn is the filter name.

Photometry ratios

PHTRATIO versus pivot wavelength is plotted in Figure 9; the ratios are similar to the detector QE ratios as shown in Figure 1. Because users of WFC3/UVIS imaging data are accustomed to using a single value for the inverse sensitivity (found in the header keyword PHOTFLAM), the calibration pipeline, CALWF3, scales by default, UVIS2 to UVIS1 via the inverse sensitivity ratio, PHTRATIO = PHTFLAM1/PHTFLAM2. The original image header keyword, PHOTFLAM is preserved and populated with the inverse sensitivity value for UVIS1, PHTFLAM1. A description of these keywords is contained in Section 7. Users who wish to preserve the chip dependent calibration can 'back out' the scaling by dividing UVIS2 by PHTRATIO. A brief description of how to reprocess WFC3/UVIS data is found in Appendix B.

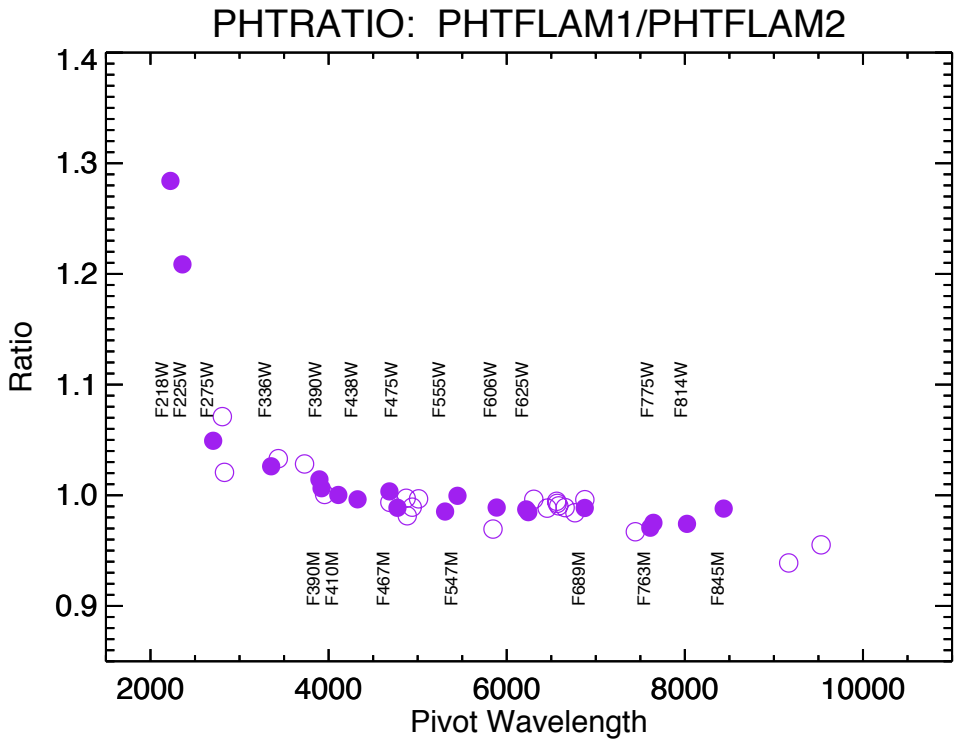

Figure 9. The ratio of the inverse sensitivities, PHTFLAM1 and PHTFLAM2, for the UVIS standard aperture with radius r=10 pixels (0.392 arcsec). The broadband and medium band filters are labeled. The ratios are largest for the two UV filters, F218W and F225W as a direct consequence of the chip QE difference at these wavelengths.

Comparison to Previous Determinations of the Inverse Sensitivities

Comparing 2016 (UVIS 2.0) to 2012 Inverse sensitivities

Comparing the chip-dependent inverse sensitivities (PHTFLAM1 and PHFTLAM2) to the calculated values for the original 'single detector' method shows that the UVIS 2.0 values are lower than the 2012 PHOTFLAM values. The average percent difference between the 2016 and 2012 inverse sensitivities for the 42 non-quad filters is -2.8% for UVIS1 and slightly more for UVIS2, -3.3%, weighted by the larger ratios in the UV. The actual range in the ratios is 0.94 to 1.01 for Chip 1 and 0.77 to 1.01 for Chip 2, with the largest percent difference being in the UV filters for Chip 2. The 2016 to 2012 ratios are plotted in Figure 10 and are consistent with the pre-launch QE differences shown in Figure 1. The largest contributor to the UVIS2 PHOTFLAM changes must be the new method of normalizing the flats to the chip2 median, rather than to chip1.

The original 2012 values of the inverse sensitivities were calculated from aperture photometry of the three white dwarfs, GD71, GD153 and G191B2B, plus the solar analog, P330E. For each

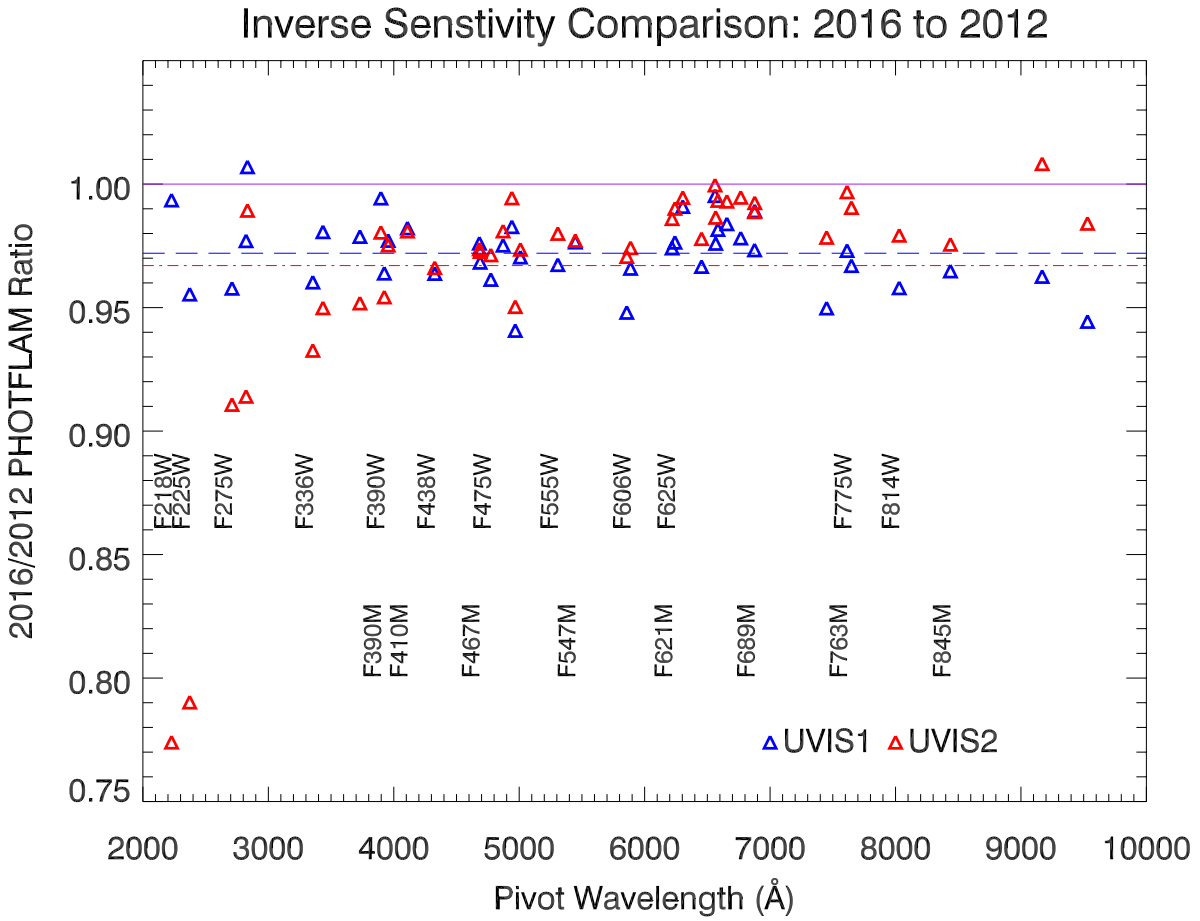

Figure 10. Comparison of the 2016 inverse sensitivity values to the 2012 values. In 2012, inverse sensitivities were calculated using 3 white dwarf stars, and 1 solar analog from combined drizzled images for each filter. Open triangles are ratios of 2016 to 2012 values. Blue triangles are for Chip1 and the blue dashed line marks the average ratio for UVIS1. Red triangles are for Chip2 and the red dot-dashed line marks the average difference for UVIS2.

star all observations in each filter (regardless of chip) were combined into a single 'master' with AstroDrizzle; cosmic ray rejection was performed by AstroDrizzle. Aperture photometry was then performed. The final results for all the stars were averaged together to calculate the inverse sensitivity, PHOTFLAM. These 2012 results made use of updated flatfields delivered in December 2011 (Mack et al. 2013) to correct for the inflight spatial sensitivity as well as a large internal optical reflection (or flare) in the ground test flats. The accuracy of these flat fields is ~1% over the full detector (Mack et al. 2015).

We expected the 2016 inverse sensitivity values to differ from the 2012 computations, but only by about 1% given that the chip-dependent values are based on observations of white dwarfs GD153, GD71 and G191B2B, only and over a longer baseline, 6 years instead of 3. However, the large discrepancy between the 2016 and 2012 inverse sensitivities is out of range.

The first check performed was to compare aperture photometry determined from the *flt.fits files multiplied by the pixel area map[5], i.e. FLT*PAM, to that from the 2016 drizzled images, finding that the photometry was identical to better than 1%. However, aperture photometry from the 2012 drizzled images differ by ~3% from the respective 2012 FLT*PAM aperture photometry, in the sense that the FLT*PAM values were brighter, strongly suggesting a problem with AstroDrizzle. We discovered that using typical AstroDrizzle configuration parameters to combine images taken at different orientations and with different signal to noise ratios can result in AstroDrizzle improperly flagging as cosmic-rays apparently discrepantly high pixel values. This subtle effect was the origin of the fainter drizzle-image aperture photometry measured in 2012 compared to the 2016 measurements.

However, the 2012 photometric calibration results were only approximately 1% different from the initial 2009 inverse sensitivity results, which had been computed slightly differently.

Comparing 2012 to 2009 Inverse sensitivities

An initial inverse sensitivity solution was derived early in the mission from data taken after launch in 2009; that analysis was based on photometry of the pipeline flt files multiplied by the pixel area map (FLT*PAM). The later 2012 inverse sensitivity solution was based on photometry of drizzled images. Differences between the final 2009 and 2012 PHOTFLAMs scatter by +/- 3% around a mean of 1.01, yet the differences between the new 2016 and 2012 solutions were unexpectedly large. For this reason, we examined the 2009 and 2012 results more closely. Figure

Table 5. Additional data used to compare 2012 to 2009 values of PHOTFLAM

Amplifier Quadrant	C512A	C512C
Program: 11426 Star: GRW+70D5824 Cycle 17/2009	F218W, F225W, F275W, F280N, F300X, F336W, F343N, F373N, F390M, F390W, F395N, F410M, F438W, F467M, F606W, F814W	F218W, F225W, F275W, F280N, F300X, F336W, F343N, F373N, F390M, F390W, F395N, F410M, F438W, F467M, F606W, F814W

[5] http://www.stsci.edu/hst/wfc3/pam/pixel_area_maps

11 shows the ratios of the 2009 to 2012 PHOTFLAM values. Broadband filters with pivot wavelengths greater than ~3500 Å have ratios hovering at ±1% while the UV filters scatter between +/- 2%. The largest scatter is seen in the narrow band filters.

The 2009 inverse sensitivities were derived from two programs, CAL/WFC3 11450, which obtained GD153 imaging data in the A amplifier only, and CAL/WFC3 11426, the UVIS contamination monitor program, which observed GRW+70 5824 with the A and C amplifier quadrants in 16 filters (Table 5). We reprocessed these data with the 2009 calibration reference files and with the 2012 reference files. Improvements in the 2012 flatfields (Mack et al. 2013) resulted in changes to the photometry, on average, by +1% in the A amp, -1.5% in the B amp, and -2% in both the C and D amplifiers. As shown in Figure 12 aperture photometry from the GRW+70 5824 FLT images confirm that the count rates in 2009 compared to those in 2012 are on average 1% lower in the A amplifier (UVIS1) and 2% higher in the C amplifier (UVIS2). More than half (between 50% - 65%, depending on filter) of the data were obtained in the A amplifier, and a simple mean would weight those observations more, masking the effect of the flat field changes. However, the effect of the 3% loss of signal in the drz photometry is not seen, but possible factors that could hide the effect are uncertainty in the initial 2009 PHOTFLAM calculations, uncertainty in the estimated encircled energy fractions, different stellar models, different flatfield normalizations, etc.

Based on the analysis described in Section 5, and in the comparison to previous determinations of WFC3/UVIS inverse sensitivities, the new chip-dependent inverse sensitivity values (i.e. PHOTFLAM) for the full-frame filters are at least 3% more accurate and have a precision of 0.8% or better.

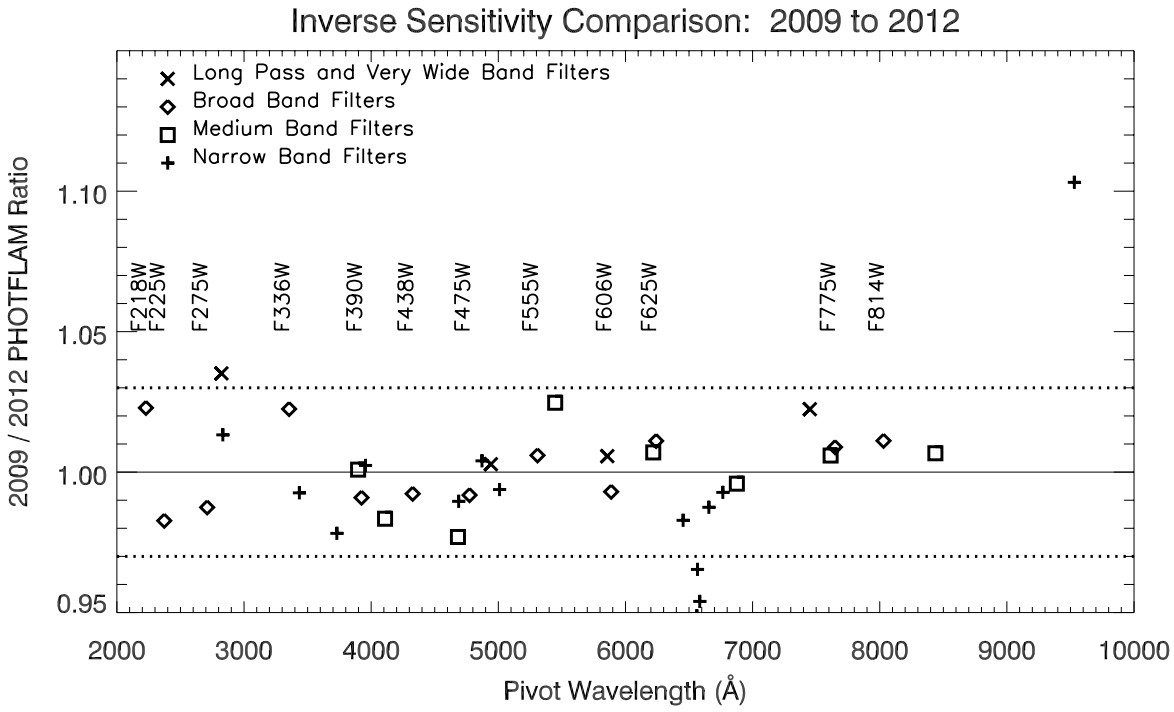

Figure 11. Ratio of the initial 2009 PHOTFLAM values to the 2012 PHOTFLAM values The broadband filters are labeled and indicated by the open diamonds.

WFC3/UVIS Color Terms

Because the inverse sensitivities are derived using hot, blue stars (white dwarfs), inverse sensitivities for redder objects may be different because of errors in the filter bandpass functions, particularly in the ultraviolet. Mack et al. (2015) used photometry of Omega Centauri to demonstrate that the UV filters have significant color terms. For example, the inverse sensitivities for blue versus red sources may be different for the two CCDs by as much as 5% in F225W.

WFC3/UVIS Photometric Transformations

Because WFC3/UVIS filters do not have an exact counterpart in any other 'standard' filter set we recommend that users refer to WFC3 photometric results in a system based on the WFC3 filters themselves. If it is absolutely necessary to compare results in different photometric systems, we recommend using synthetic photometry. The transformation of observed magnitudes to a standard system is an approximation but suffices for some applications.

For ground-based data, most of the error comes from the atmospheric transmission coefficients, and to a lesser extent from changes in the system throughputs (which are not always documented) rather than the source characteristics. Therefore transformation coefficients calculated using synthetic stellar models are generally adequate for most purposes. Sahu, Deustua and Sabbi (2014) provide a recipe for deriving the required transformation coefficients using the SYNPHOT *calcphot* task in PyRAF/IRAF.

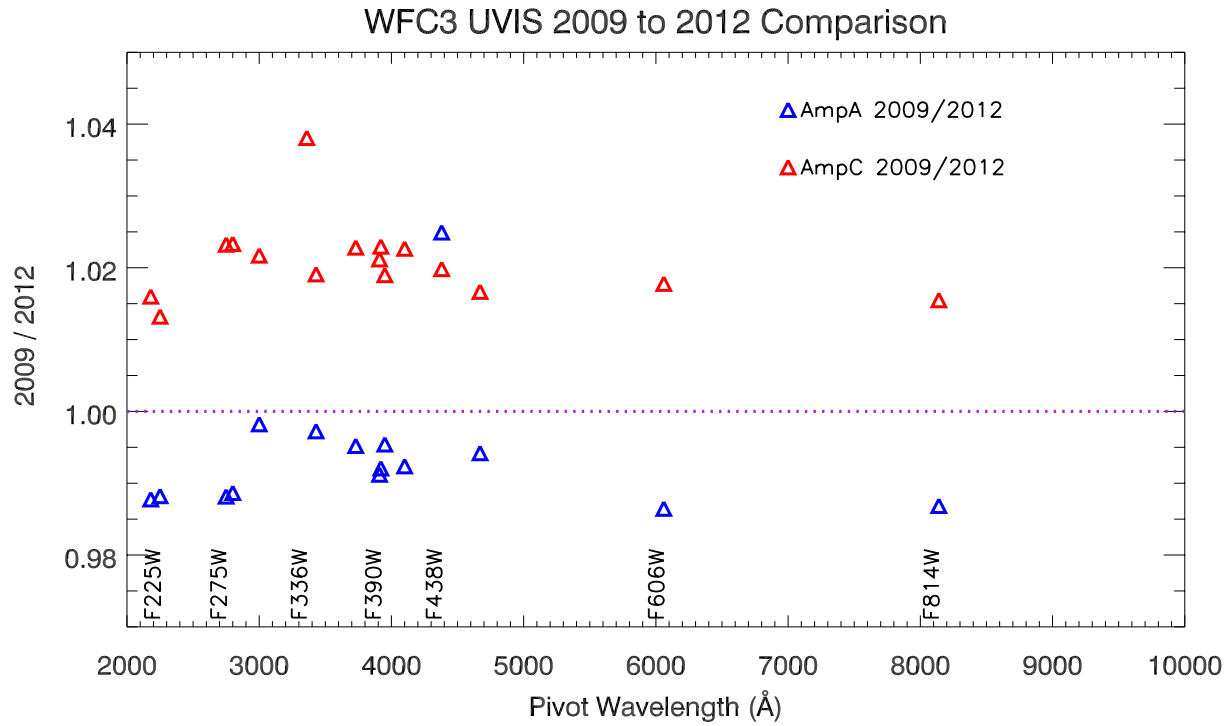

Figure 12. WFC3 UVIS 2009 / 2012 count rate ratios for Amp A and Amp C, for a 0.4 arcsec aperture radius. The 2009 data were processed using ground flats, obtained before launch. In 2012 new, inflight flatfields were created, and these were used to reprocess all the images obtained between 2009 and 2012. If there were no changes to the flat fields files the ratio would be near 1 for each amplifier.

7. Error analysis

For each image, the statistical uncertainty at each aperture radius is calculated under the assumption that each source of noise, N_i, is independent, thus can be summed in quadrature:

$$N^2 = \sum N_i^2 \qquad \text{Equation 5}$$

Following Newberry (1991), the total noise in the aperture is

$$N^2 = C_{obj} + npix\left(f_{sky} + A^2\right) + \frac{npix}{nsky}\left(f_{sky} + A^2\right) \qquad \text{Equation 6}$$

$$A^2 = RN^2 + T^2 + (Processing\ Noise)^2 \qquad \text{Equation 7}$$

where C_{obj} is the source signal, f_{sky} is the average sky signal, npix is the number of pixels in the aperture, nsky is the number of pixels used to determine the average sky signal, A is the sum of the noise due to readnoise (RN), gain (T), processing noise from dark current, bias and dark subtraction, flat fielding , and intrinsic repeatability. All units are in electrons.

For large aperture photometry the sky and processing noise become important. .Exposure times are short for our bright standards stars, and hence the background sky signal per pixel is small. For exposures taken using FLASH, the background signal is ~12 e-/pixel, is still smaller compared to the source signal and is corrected during pipeline processing. The gain noise, T, is negligible at 0.046 e-/DN.

Khandrika (2015) determined the UVIS readnoise to be of 2.97, 3.03, 2.95, 3.06 electrons for Amps A, B, C and D respectively. The read noise changed by ~ 0.045 e- from its 2009 values. We use the average readnoise value of RN =3 e-. The dark current for the two WFC3 CCDs while not identical, are similar in terms of the rate of increase. In 2009, the dark currents were approximatel 1.5 e-/hr and 2.1 e-/h for UVIS1 and UVIS2 respectively. In 2015, the dark current was ~5.3 e-/hr for UVIS1 and ~5.5 e-/hr for UVIS2. We use an average dark current of 4.4 e-/hr for UVIS1 and 5 e-/hr for UVIS2 for the time period between 2009 and 2015. The second term, npix(fsky+dark+RN^2), is less than 0.05% of the signal, and hence negligible.

Bohlin found ~0.4% repeatability error for ACS, which could be due to small differences in the placement of the stars along with small flat field errors. We find repeatability between 0.4% and 0.8%. A conservative estimate of 0.8% is assumed for the sum of all other sources of noise including the flat fields and repeatability. Third term in the equation: npix/nsky(f_{sky}+A^2) $\leq$ (0.008 x C_{obj})^2 and Equation 6 becomes

$$N^2 = C_{obj} + (0.008C_{obj})^2 \qquad \text{Equation 8}$$

As an example, ibcda7vaq_flt.fits is a 2.9 second exposure of GD153 in F606W. In an r=10 pixel aperture, npix=314.2 pixels and C_{obj} = 297287.7 electrons, corresponding to a count rate of 102513.3 e-/s. The mean sky is f_{sky}=2.3 electrons (0.79 e-/s) measured in an annulus between r=152 to r=197 pixels, over nsky=24692 pixels. The dark current for this exposure is 0.0044 e-. The poisson noise is 0.18% of C_{obj}, N^2 = 5.9572E+06, and so N=2440.7 corresponding to 0.82% of C_{obj}.

Table 6. Uncertainties for UVIS1 and UVIS2 aperture photometry at radius r=10 pixels (0.3962 arcsec)

	UVIS1				UVIS2			
Filter	No. Stars	No. Images	RMS	Error in the mean	No. Stars	No. Images	RMS	Error in the mean
F200LP	1	2	0.0102	0.0072	1	4	0.0088	0.0044
F218W	2	10	0.0117	0.0037	2	10	0.0118	0.0037
F225W	3	44	0.0132	0.0020	3	18	0.0136	0.0032
F275W	3	44	0.0132	0.0020	3	18	0.0136	0.0032
F280N	2	8	0.0126	0.0045	2	4	0.0135	0.0068
F300X	1	6	0.0086	0.0035	2	6	0.0120	0.0049
F336W	3	44	0.0132	0.0020	3	18	0.0136	0.0032
F343N	2	8	0.0121	0.0043	2	4	0.0127	0.0064
F350LP	3	44	0.0132	0.0020	2	12	0.0138	0.0040
F373N	2	8	0.0130	0.0046	2	4	0.0140	0.0070
F390M	2	6	0.0127	0.0052	2	4	0.0129	0.0065
F390W	3	42	0.0132	0.0020	3	14	0.0138	0.0037
F395N	1	6	0.0086	0.0035	2	4	0.0130	0.0065
F410M	2	8	0.0123	0.0043	2	4	0.0130	0.0065
F438W	3	44	0.0132	0.0020	3	20	0.0140	0.0031
F467M	2	12	0.0116	0.0033	3	38	0.0135	0.0022
F469N	2	12	0.0121	0.0035	3	38	0.0137	0.0022
F475W	3	48	0.0131	0.0019	2	22	0.0139	0.0030
F475X	2	8	0.0117	0.0041	1	6	0.0120	0.0049
F487N	2	8	0.0126	0.0045	2	4	0.0136	0.0068
F502N	2	12	0.0121	0.0035	3	38	0.0137	0.0022
F547M	2	14	0.0113	0.0030	3	42	0.0133	0.0021
F555W	3	44	0.0132	0.0020	3	20	0.0140	0.0031
F600LP	2	8	0.0119	0.0042	2	8	0.0119	0.0042
F606W	2	10	0.0114	0.0036	3	52	0.0135	0.0019
F621M	2	10	0.0117	0.0037	2	8	0.0121	0.0043
F625W	2	10	0.0115	0.0036	2	10	0.0118	0.0037
F631N	2	4	0.0139	0.0070	2	4	0.0139	0.0070
F645N	2	8	0.0127	0.0045	2	4	0.0137	0.0069
F656N	2	8	0.0130	0.0046	2	4	0.0138	0.0069
F657N	2	4	0.0137	0.0069	1	4	0.0137	0.0069
F658N	2	8	0.0130	0.0046	1	4	0.0137	0.0069
F665N	2	8	0.0125	0.0044	1	4	0.0137	0.0069
F673N	2	8	0.0128	0.0045	1	4	0.0138	0.0069
F680N	2	4	0.0130	0.0065	1	4	0.0130	0.0065
F689M	2	8	0.0123	0.0043	1	4	0.0130	0.0065
F763M	2	8	0.0127	0.0045	1	4	0.0135	0.0068
F775W	2	6	0.0121	0.0049	1	6	0.0121	0.0049
F814W	2	6	0.0120	0.0049	3	20	0.0136	0.0030
F845M	2	10	0.0120	0.0038	1	6	0.0125	0.0051
F850LP	3	38	0.0137	0.0022	1	20	0.0139	0.0031
F953N	2	8	0.0140	0.0049	1	4	0.0156	0.0078

Table 6 lists the RMS error, the error in the mean for each detector and each filter, as well as the number of FLT images and number of stars per filter+detector used in the calculation. The total

noise is derived for the number of individual FLT images used to determine the encircled energy fraction, and therefore the photometry, for the r=10 pixel circular aperture; noise is calculated as a percentage of the source counts (in electrons) and summed in quadrature to obtain the total noise. Exposures range in signal to noise from SNR =100 up to SNR ~700, thus the rms is somewhat larger than 1%. The error in the mean is obtained by dividing the rms by the square root of number of individual images. For UVIS1 the rms is 1.23%, and for UVIS2 it is 1.32

8. Changes to Image Processing: CALWF3, Reference Files, Keywords.

The new chip-dependent solutions (flats and inverse sensitivities) represent a significant change in the photometric calibration of the WFC3/UVIS channel. It required modifying CALWF3 (the WFC3 reduction pipeline) to independently process each CCD, populate new keyword values, and properly normalize the two chips based on the inverse sensitivity ratio. These significant changes are transparent to the user performing photometry on archival data products. **Users should remember that that PHOTFLAM is now defined at the smaller standard aperture, so users may see a 10% difference if they aren't careful!** UVIS 2.0 also implements sink pixel flagging (Anderson and Baggett, 2014), as well as a pixel-based charge transfer efficiency[6] correction (CTE; Anderson and Bedin, 2010). CTE losses have negligible effects, <0.1% on bright stars placed near the amplifiers (Baggett, Gosmeyer and Noeske, 2015).

The updated calwf3, version 3.3 data products are:

*_flt.fits, *_drz.fits (bias, dark, flatfield corrected, and also drizzled for the drz)

*_flc.fits, and *_drc.fits (as above and CTE-corrected)

Changes specific to photometry are new keywords, new calibration switches and a new structure to the photometry reference file (IMPPHTAB). These are described below.

Header Keywords

Three new keywords are added to the image headers:

PHTFLAM1= inverse sensitivity for UVIS1 + filter for 10 pixel radius

PHTFLAM2= inverse sensitivity for UVIS2 + filter for 10 pixel radius

PHTRATIO = PHTFLAM2/PHTFLAM1

Prior to 2016, the values for PHOTFLAM, the original, 'single detector' inverse sensitivity keyword, were provided for the infinite aperture. Starting in 2016, the PHOTFLAM keyword is retained, but the value now is for the UVIS1 inverse sensitivity at r=10 pixel (0.3962 arcsec) aperture, i.e. identical to PHTFLAM1.

[6] General information about CTE can be found in the white paper by MacKenty and Smith (2012)

Table 7. New IMPHTTAB File Structure

EXT#	FITSNAME	FILENAME	Description
0	NEW_IMP.FITS	NEW_IMP.FITS	Primary header
1	BINTABLE	PHOTFLAM	Inverse sensitivity for UVIS1 (= PHTFLAM1) ergs-cm^{-2}-A^{-1}-electron^{-1}
2	BINTABLE	PHOTPLAM	Filter pivot wavelength, Å
3	BINTABLE	PHOTBW	Filter Bandwidth, Å
4	BINTABLE	PHTFLAM1	Inverse sensitivity for UVIS1
5	BINTABLE	PHTFLAM2	Inverse sensitivity for UVIS2

CALWF3 Processing Switches

CALWF3 version 3.3 is modified to process each CCD independently. Two new calibration switches are implemented, PHOTCORR and FLUXCORR, and must be set to PERFORM, for calwf3 to process the chip-dependent reduction.

```
PHOTCORR = PERFORM      PHTRATIO is calculated and PHOTFLAM, PHTFLAM1 and
                        PHTFLAM2 keywords are populated in the header
FLUXCORR= PERFORM       Chip 2 is scaled to Chip1 (i.e. UVIS2*PHTRATIO)
```

The UVIS 2.0 implementation of CALWF3 normalizes UVIS2 (Chip2) to UVIS1 (Chip1) via the ratio of the CCD inverse sensitivity, PHTRATIO, defined as PHTFLAM2/PHTFLAM1. Most users of UVIS 2.0 data will, therefore, only need one inverse sensitivity value (PHTFLAM1), which, is copied to the original (pre-2016) inverse sensitivity header keyword, PHOTFLAM (calculated for r=10 pixels). Users who wish to do so can 'back out' the CALWF3 normalization, and then apply the chip specific values, PHTFLAM1 for UVIS1 (Chip1) and PHTFLAM2 for UVIS2 (Chip2), after making any necessary aperture corrections. Subarray data obtained with UVIS2 (chip 2) will be scaled by the PHTRATIO (if FLUXCORR=PERFORM) to ensure objects have the same signal regardless of the chip on which they were observed. This also means that users only need to keep track of a single set of inverse sensitivities values.

Reference File: New IMPHTTAB

CALWF3 reads a reference file of photometric values, the IMPHTTAB, to obtain the inverse

Table 8 Structure of the IMPHTTAB extensions

Column	1	2	3	4	5
EXT1	OBSMODE	DATACOL	PHOTFLAM	PEDIGREE	DESCRIP
EXT2	OBSMODE	DATACOL	PHOTPLAM	PEDIGREE	DESCRIP
EXT3	OBSMODE	DATACOL	PHOTBW	PEDIGREE	DESCRIP
EXT4	OBSMODE	DATACOL	PHTFLAM1	PEDIGREE	DESCRIP
EXT5	OBSMODE	DATACOL	PHTFLAM2	PEDIGREE	DESCRIP
Format	CH*40	CH*12	D(25.16g)	CH*30	CH*110

sensitivity values. To handle the two-chip solution, the IMPHTTAB file structure was changed by adding two extensions, so that now there are five, each of which is a binary table, as described in Table 7. This format was adopted to be compatible with the current pipeline software's cross-instrument implementation of photometric calculations. Table 8 provides information on the structure of each bintable. Extensions 1, 4 and 5 share the same format, Extension 2 and Extension 3 are exactly like the 'single detector' version and contain the pivot wavelength and bandwidth for the two CCDs respectively. Observing modes (e.g. wfc3, uvis2, f606w) for the CCDS are listed in the OBSMODE column in Extensions 1, 4 and 5. As discussed previously the PHOTFLAM values (EXT 1) are identical to PHTFLAM1 (EXT 4). In EXT 4, the PHTFLAM1 values for UVIS2 modes are set to zero, and in EXT 5, the PHTFLAM2 values for UVIS1 modes are set to zero.

The Synphot/PySynphot files are updated and described in more detail in Deustua (2016). Synphot files can be downloaded from the CRDS.

9. Conclusions

We compute new inverse sensitivity values for each WFC3/UVIS CCD+filter, PHTFLAM1 and PHTFLAM2, from the new chip-dependent flat fields and encircled energy fractions, and updated white dwarf stellar models. These inverse sensitivities are computed from the three standard white dwarfs, G191B2B, GD153, and GD71, using 6 years of observations. They are 3% more accurate than previous estimates, and have statistical uncertainty less than 1%.

Comparison with previous inverse sensitivities determinations with the previous 2012 inverse sensitivities revealed a ~3% offset. The difference was traced to subtleties when using AstroDrizzle to process images with different signal to noise and orientation in 2012. These effects produced systematically low aperture photometry count rates, which resulted in inverse sensitivities systematically ~3% too high. The new 2016 inverse sensitivities are computed from data processed to avoid these effects and, as such, represent the optimum solution at this time.

Changes in the structure of the photometry reference file, IMPHTTAB, were made to accommodate the chip-dependent processing. New photometry keywords are added to the image headers. For the most part, these changes are transparent to users, who will only need to keep track of a single set of inverse sensitivities (for UVIS1), as before.

Values in the PHOTFLAM keyword are provided for an r=10 pix aperture, NOT for an infinite aperture, so users need to apply the appropriate aperture corrections to their photometry. For extended sources, correction to the infinite aperture of radius=6 pixels using the EE tables is required.

Acknowledgements

We thank Ralph Bohlin for carefully reviewing this ISR, and whose suggestions and comments greatly improved this report. Many thanks to the entire WFC3 team for their contributions to the work presented here.

10. References

Anderson, J. and Bedin, L., 2010, *An Empirical Pixel Based Correction for Imperfect CTE. I. HST's Advanced Camera for Surveys*, PASP, 122, 1035

Anderson, J., and Baggett, S., 2014, "*Flagging the Sink Pixels in WFC3/UVIS*", WFC3 ISR 2014-22.

Baggett, S., Gosmeyer, C., Noeske, K., 2015, "*WFC3/UVIS Charge Transfer Efficiency 2009-2015*", WFC3 ISR 2015-003.

Baggett, S., 2007, WFC3 ISR 2007-14 http://www.stsci.edu/hst/wfc3/documents/ISRs/WFC3-2007-14.pdf

Bajaj, V., 2016, *The Updated Calibration Pipeline for WFC3/UVIS: A Cookbook to Calwf3 3.3,* WFC3 ISR 2016-02.

Bowers, A.S., Mack, J., and Deustua, S., 2016, *UVIS2.0 Encircled Energy* (in preparation), WFC3 ISR 2016-06.

Bohlin, R.C, 2014, *Hubble Space Telescope CALSPEC Flux Standards: Sirius (and Vega*), AJ,147,127

Bohlin, R.C. 2016, *Perfecting the Photometric Calibration of the ACS CCD Cameras, AJ, 152, 60*

Bohlin, Ralph C.; Gordon, Karl D.; Tremblay, P. -E. 2014, *Techniques and Review of Absolute Flux Calibration from the Ultraviolet to the Mid-Infrared,* PASP, 126, 711

Clampin, M., Hartig, G.F., Ford, H.C., Sirianni, M., Purdue, G., Walkowicz, L., Golimowski, D.A., Illingworth, G., Blouke, M., Lesser, M., Burmester, B., Kimble, R., Sullivan, P., and, Krebs, C., 1998, *CCD Detectors for the Advanced Camera for Surveys*, SPIE, 3356, 332.

Deustua, S., 2016, *Updated SYNPHOT/PYSYNPHOT Files*, WFC3 ISR-2016-04

Dressel, L., 2016. *Wide Field Camera 3 Instrument Handbook, Version 8.0"* (Baltimore: STScI)

Griffith, R., editor, 1992, WF/PC Instrument Handbook, Version 3, (Baltimore: STScI) http://www.stsci.edu/hst/wfpc/documents/HST_WFPC_Instrument_Handbook.pdf

Hartig, G.F., 2009, *WFC3 SMOV Programs 11436/8: UVIS On-orbit PSF Evaluation,* WFC3 ISR 2009-38.

Holtzman, J.A., Burrows, C.J., Casertano, S., Hester, J.J., Trauger, J.T., Watson, A.M., and Worthey, G., 1995, *The Photometric Performance and Calibration of WFPC2,* PASP, 107, 1065.

Kalirai, J.S., Baggett, S., Borders, T., and Rajan, A., 2010, *The Photometric Performance of WFC3/UVIS: Temporal Stability Through Year 1,* WFC3 2010-14.

Mack, J., 2016, *UVIS 2.0 Ultraviolet Flats* (in preparation), WFC3 ISR-2016-05.

Mack, J., Dahlen, T., Sabbi, E., and Bowers, A. S., 2016, UVIS *2.0: Chip-Dependent Flats,* WFC3 ISR 2016-04.

Mack, J., Rajan, A., & Bowers, A. 2015, "*Spatial Accuracy of the UVIS Flat Fields*", WFC3 ISR 2015-18.

Mack, J., Sabbi, E., and Dahlen, T., 2013, '*In-flight Corrections to the WFC3 UVIS Flat Fields,* WFC3 ISR 2013-10.

MacKenty, J. and Smith, L.*, 2012, CTE White Paper*, http://www.stsci.edu/hst/wfc3/ins_performance/CTE/CTE_White_Paper.pdf

Malamuth, E., et al, 2003, *Model of Fringing in the WFC3 CCD*s, SPIE, 4854, pp. 567-576

Martlin, C and Gunning, H., 2016, *WFC3 Cycle 22 Proposal 14009: UVIS Gain,* WFC3 ISR-2016-09

Rauch, T, Werner, K., Bohlin, R., and Kruk, J.W., 2013, *The virtual observatory service TheoSSA: Establishing a database of synthetic stellar flux standards I. NLTE spectral analysis of the DA-type white dwarf G191−B2B,* A&A, 560, A106

Ryan Jr. R. E., Deustua, S., Anderson, J., et al., 2016, *The Updated Calibration Pipeline for WFC3/UVIS: A Reference Guide to Calwf3 3.3,* WFC3 ISR 2016-01.

Sabbi E., Mack, J., Pirzkal, N., Viana, A., and Kalirai, J.S., 2010, WFC3 UVIS and IR flat-fields, in S. Deustua and C. Oliveira, eds, 2010 HST Calibration Workshop Proceedings, Space Telescope Science Institute. http://www.stsci.edu/~INS/2010CalWorkshop/sabbi.pdf

Sabbi, E. & Bellini, A., 2013, *UVIS PSF Spatial & Temporal Variations* WFC3 ISR- 2013-11.

Sirianni, M. and Clampin, M., 2000, *Status of WFC Build-4 CCDs*. Technical report. http://adcam.pha.jhu.edu/instrument/detectors/WFC/builds/4/Statuswfc4.pdf

Smith, E., et al. 2011*, "Introduction to the HST Data Handbooks", Version 8.0*, (Baltimore: STScI). *http://www.stsci.edu/hst/HST_overview/documents/datahandbook/*

Wong, M., 2010, *Amplitude of fringing in WFC3/UVIS narrowband red filters,* WFC3 ISR 2010-04.

Appendix A: UVIS1 and UVIS2 Inverse Sensitivity (PHOTFLAM) and Encircled Energy Fraction Tables

Chip-dependent inverse sensitivities for UVIS1 and UVIS2 are calculated for an aperture with radius = 10 pixels (0.3962 arcsec) for the 42 full frame filters. Table 9 and Table 10 list the values at r=10 pixels for UVIS1 and UVIS2 respectively. The inverse sensitivities are based on the three white dwarf standard stars: GD71, GD153, G191B2B, consistent with the inverse sensitivity determinations for ACS, STIS, and NICMOS.

Quad filter values are unchanged from 2012, and are listed in Table 10 for the r=10 pixel aperture (0.3962 arcsec). Their inverse sensitivity values remain the same, as the quad filter flatfields are not updated. The quad filters still make use of the pre-flight flats that contain the flare. Once the inflight correction is available, the inverse sensitivities for these filters will be recomputed.

Users who measure photometry at other aperture radii will need to apply the appropriate aperture corrections to these inverse sensitivities, using the EE fractions, as in the example below.
Table 12 provides the multiplicative factors by which the PHOTFLAM (or PHTFLAM1 or PHTFLAM2) is multiplied to obtain the value of the inverse sensitivity at that radius:

$$\text{PHOTFLAM (3 pixels)} = \text{PHOTFLAM} \times \text{MF},$$

where PHOTFLAM is the inverse sensitivity from Table 8 for UVIS1, Table 9 for UVIS2 or Table 10 for the quad filters. The multiplicative factor, MF = EE(r10)/EE(r), i.e. the ratio of encircled energy fractions, as in the following example. The infinite aperture radius that is required for the diffuse source specific intensity calibration is defined at 6 arcsec (151 pixels).

For example, if one uses an aperture with radius r=3 pixels, on sources taken with the F606W filter on UVIS1, the corresponding value of PHOTFLAM (from Table 9) is

$$\text{PHOTFLAM (3 pixels)} = 1.24510\text{E-}19 \times 1.226 = 1.52649\text{E-}19 \ \text{erg cm}^{-2}\ \text{A}^{-1}\ \text{e}^{-1}$$

The EE fractions derived from the 'master' images are the same for UVIS1 and UVIS2, and are less than 0.1% different from EE fractions derived directly from flt images at radii r > 5 pixels. For smaller radii the flt derived EE fractions are 3% larger at r=2 pixels, 1% at r=4 pixels. Therefore, only <u>one set</u> of filter-dependent encircled energy values from the master drizzled images are listed in Table 13 through Table 17. In Table 18 we provide, for convenience, the Hartig (2009) updated model values and in Table 19 the measured PSF values (Hartig, private communication) are given.

Photometric Systems

VEGAmag: In this system, Vega (Alpha Lyra) by definition has magnitude 0 at all wavelengths. The Vega magnitude of a star with flux F is

$$m_{vega} = -2.5 \log10 (F/F_{vega})$$

where F_{vega} is the absolute CALSPEC flux of Vega; and for photometry, the fluxes must be averaged over the bandpass. (See Bohlin et al. 2014) for the equations that define the average flux.)

STmag and ABmag: both systems define an equivalent flux density for a source, corresponding to the flux density of a source of predefined spectral shape that would produce the observed count rate, and convert this equivalent flux to a magnitude. The conversion is chosen so that the magnitude in V corresponds roughly to that in the Johnson system.

In the STmag system, the flux density is expressed per unit wavelength, and the reference spectrum is flat in F_{λ}. In the ABmag system, the flux density is expressed per unit frequency, and the reference spectrum is flat in F_{ν}. The definitions are:

$$STmag = -2.5 \log F_{\lambda} - 21.10$$

$$ABmag = -2.5 \log F_{\nu} - 48.6$$

where F_{ν} is expressed in erg cm^{-2} s^{-1} Hz^{-1}, and F_{λ} in erg cm^{-2} s^{-1} $Å^{-1}$. An object with F_{ν} = 3.63 x 10^{-20} erg cm^{-2} s^{-1} Hz^{-1} will have magnitude AB =0 in every filter, and an object with F_{λ} = 3.63 x 10^{-9} erg cm^{-2} s^{-1} $Å^{-1}$ will have STmag=0 in every filter.

How to use the photometry and encircled energy tables:

For drizzled images, or flat-fielded images multiplied by the pixel area map (i.e. FLT*PAM), the mean signal in a circular aperture of radius r is:

$$Flux = FI * PHOTFLAM * EE(r10)/ EE(r)$$

Where FI is the signal within aperture r in electrons per second, EE(r10) is the encircled energy fraction at r=10 pixels EE(r) is the encircled energy fraction at radius r. PHOTFLAM is the inverse sensitivity at r=10 pixels, whose default value is PHOTFLM1. Substitute PHOTFLAM2 for UVIS2, for example if the data were processed with FLUXCORR set to OMIT.

The equivalent calculation using magnitudes is:

$$m=mi - 2.5*\log[EE(r10)/EE(r)] + ZP$$

where mi is the instrumental magnitude, mi = -2.5*log(FI), ZP (in mag) is the PHOTFLAM equivalent in mags from Tables 8-10, and EE(r10) and EE(r) are as above.

Example:

Aperture photometry using a *drz.fits image, for radius r=3 pixels of a star on the UVIS1 CCD with the F606W filter yields FI=950 electrons/second.

The inverse sensitivity of F606W is PHTFLAM1 = 1.2451E-19 erg-s^{-1}-cm^{-2}-A^{-1} per e^{-}-s^{-1} (from Table 8). The encircled energy at r= 3 pixels and at r=10 pixels from Table 12:

$$EE(r=3) = 0.7417 \text{ (UVIS1)}$$

$$EE(r=10)=0.910 \text{ (UVIS1)}$$

*In physical units: Flux= 950 * 1.2451E-19 * 0.912/0.7547 = 1.45125E-16 erg-s^{-1}-cm^{-2}-A^{-1}*
*In VEGAMAG: m=-2.5log(950) + 25.912 -2.5*log(0.910/0.7417) = 18.246 mag*

NOTE: Photometry at r<8 pixels relative to r=10 pixels can vary, depending on focus and breathing. At r=3 pixels, the variation is between 4% -10% (see Sabbi & Bellini WFC3-ISR-2013-011).

Table 9 Inverse Sensitivity Values for UVIS1 calculated for r=10 pixels (0.3962 arcsec).

UVIS1	PHOTPLAM Å	PHOTBW Å	PHTFLAM1 erg cm^{-2} A^{-1} e^{-1}	STMAG mag	ABMAG mag	VEGAMAG mag
F200LP	4973.7	1755.4	5.27457E-20	27.095	27.303	26.819
F218W	2227.3	128.3	1.68899E-17	20.831	22.784	20.997
F225W	2370.7	177.2	5.26429E-18	22.097	23.914	22.165
F275W	2708.7	164.3	3.65179E-18	22.494	24.022	22.467
F280N	2832.2	198.5	6.50653E-17	19.367	20.798	19.311
F300x	2816.5	315.0	1.59499E-18	23.393	24.837	23.366
F336W	3353.7	158.4	1.42182E-18	23.518	24.582	23.387
F343N	3434.9	86.7	2.82680E-18	22.772	23.784	22.623
F350LP	5907.9	1514.8	5.51786E-20	27.046	26.881	26.710
F373N	3730.8	18.4	1.48145E-17	20.973	21.806	20.871
F390M	3897.1	65.5	2.79003E-18	22.786	23.524	23.433
F390W	3921.9	291.4	5.46738E-19	24.556	25.280	25.056
F395N	3955.2	26.3	6.50556E-18	21.867	22.573	22.591
F410M	4108.9	57.2	2.56278E-18	22.878	23.502	23.648
F438W	4325.6	197.3	7.32257E-19	24.238	24.750	24.891
F467M	4682.5	68.7	1.80172E-18	23.261	23.600	23.746
F469N	4688.7	20.1	1.01558E-17	21.383	21.720	21.867
F475W	4771.5	421.4	2.70287E-19	25.320	25.619	25.705
F475x	4938.3	661.3	1.65667E-19	25.852	26.076	26.116
F487N	4872.0	21.8	6.38151E-18	21.888	22.141	21.934
F502N	5009.6	27.1	5.57769E-18	22.034	22.227	22.302
F547M	5447.5	206.3	4.96751E-19	24.660	24.671	24.665
F555W	5308.6	518.2	1.98117E-19	25.658	25.725	25.741
F600LP	7506.4	964.9	9.18068E-20	26.493	25.808	25.472
F606W	5892.5	658.5	1.24510E-19	26.162	26.003	25.912
F621M	6219.3	185.7	4.35790E-19	24.802	24.525	24.373
F625W	6245.1	451.8	1.84801E-19	25.733	25.448	25.293
F631N	6304.9	42.3	5.22516E-18	22.105	21.798	21.634
F645N	6453.6	42.0	3.58138E-18	22.515	22.158	21.962
F656N	6562.8	42.3	1.77620E-17	20.776	20.383	19.760
F657N	6566.7	41.1	2.38263E-18	22.957	22.563	22.231
F658N	6585.4	151.0	1.05217E-17	21.345	20.944	20.592
F665N	6655.9	42.2	2.16090E-18	23.063	22.639	22.396
F673N	6766.0	42.0	2.40593E-18	22.947	22.487	22.242
F680N	6877.9	112.0	7.58232E-19	24.200	23.705	23.442
F689M	6877.7	207.7	4.04561E-19	24.883	24.387	24.104
F763M	7616.1	229.6	4.18481E-19	24.846	24.129	23.744
F775W	7657.6	421.0	2.26784E-19	25.511	24.783	24.394
F814W	8059.5	673.8	1.63049E-19	25.869	25.030	24.603
F845M	8442.3	260.7	5.00830E-19	24.651	23.711	23.204
F850LP	9191.2	476.5	4.03933E-19	24.884	23.759	23.232
F953N	9530.7	69.3	8.90833E-18	21.526	20.322	19.702

Table 10 Inverse Sensitivity Values for UVIS2 calculated for r=10 pixels (0.3962 arcsec).

UVIS2 Filter	PHOTPLAM Å	PHOTBW Å	PHTFLAM2 erg cm^{-2} A^{-1} e^{-1}	STMAG mag	ABMAG mag	VEGAMAG mag
F200LP	4882.8	1741.6	5.32873E-20	27.083	27.332	27.253
F218W	2222.9	124.4	1.31586E-17	21.102	23.059	21.178
F225W	2356.9	172.8	4.35417E-18	22.303	24.133	22.277
F275W	2702.2	165.4	3.47244E-18	22.548	24.082	22.493
F280N	2829.3	200.5	6.39262E-17	19.386	20.820	19.360
F300X	2801.5	315.2	1.49219E-18	23.465	24.921	23.335
F336W	3353.9	158.3	1.38091E-18	23.550	24.614	23.400
F343N	3435.0	86.6	2.73804E-18	22.806	23.819	22.474
F350LP	5895.7	1513.3	5.64935E-20	27.020	26.859	26.918
F373N	3730.8	18.3	1.44068E-17	21.004	21.837	21.650
F390M	3896.9	65.5	2.75122E-18	22.801	23.540	23.299
F390W	3918.9	291.3	5.41283E-19	24.566	25.293	25.291
F395N	3955.1	26.3	6.49305E-18	21.869	22.575	22.639
F410M	4108.8	57.2	2.55950E-18	22.880	23.503	23.532
F438W	4324.5	197.5	7.34039E-19	24.236	24.748	24.721
F467M	4682.6	68.7	1.79741E-18	23.263	23.603	23.747
F469N	4688.7	20.2	1.02015E-17	21.378	21.715	21.764
F475W	4770.8	422.0	2.73086E-19	25.309	25.608	25.574
F475X	4935.7	662.0	1.67632E-19	25.839	26.064	25.885
F487N	4872.0	22.0	6.41917E-18	21.881	22.135	22.149
F502N	5009.6	27.3	5.59575E-18	22.030	22.223	22.035
F547M	5447.4	206.2	4.97105E-19	24.659	24.670	24.742
F555W	5308.7	518.1	2.00706E-19	25.644	25.711	24.626
F600LP	7499.6	959.9	9.45714E-20	26.461	25.778	26.210
F606W	5892.5	658.5	1.25588E-19	26.153	25.993	25.723
F621M	6219.7	185.8	4.41115E-19	24.789	24.512	24.348
F625W	6245.4	451.8	1.87396E-19	25.718	25.432	25.248
F631N	6304.9	43.2	5.24451E-18	22.101	21.794	21.548
F645N	6453.6	42.9	3.62324E-18	22.502	22.145	21.486
F656N	6562.8	42.9	1.78391E-17	20.772	20.378	20.045
F657N	6566.7	41.1	2.40842E-18	22.946	22.551	22.193
F658N	6585.3	153.2	1.06479E-17	21.332	20.931	20.665
F665N	6655.9	42.3	2.18101E-18	23.053	22.629	22.349
F673N	6765.9	42.2	2.44650E-18	22.929	22.469	22.170
F680N	6877.7	112.1	7.60745E-19	24.197	23.702	23.419
F689M	6877.7	207.9	4.10969E-19	24.865	24.370	23.764
F763M	7614.9	229.1	4.28698E-19	24.820	24.103	23.704
F775W	7655.8	419.9	2.32295E-19	25.485	24.757	24.220
F814W	8054.0	672.7	1.66670E-19	25.845	25.007	24.399
F845M	8441.1	260.1	5.06451E-19	24.639	23.699	22.987
F850LP	9187.9	473.7	4.23086E-19	24.834	23.710	23.010
F953N	9530.7	70.2	9.28301E-18	21.481	20.277	19.66

Table 11. Inverse Sensitivity Values for the Quad Filters calculated for r=10 pixels

UVIS FILTER	UVIS CCD	PHOTPLAM	PHOTBW	PHOTFLAM	STmag	ABmag	VEGAmag
		Å	Å	erg cm^{-2} A^{-1} e^{-1}	mag	mag	mag
FQ422M	2	4219.20	38.33	5.53708e-18	22.0418	22.6078	22.8487
FQ232N	2	2432.20	263.50	1.76489e-16	18.2832	20.0453	18.4139
FQ243N	2	2476.40	194.01	1.32499e-16	18.5945	20.3175	18.6672
FQ378N	1	3792.40	32.15	6.48351e-18	21.8704	22.6680	22.1859
FQ387N	1	3873.60	15.01	2.23500e-17	20.5268	21.2783	21.1941
FQ436N	2	4367.10	22.82	1.32831e-17	21.0917	21.5829	21.6211
FQ437N	1	4371.00	21.61	1.86629e-17	20.7226	21.2118	21.3279
FQ492N	1	4933.40	35.18	3.42639e-18	22.5629	22.7892	22.8564
FQ508N	1	5091.00	42.38	3.27047e-18	22.6135	22.7716	22.8444
FQ575N	2	5757.70	42.20	1.98563e-17	20.6553	20.5461	20.4865
FQ619N	1	6198.50	36.45	5.14293e-18	22.1220	21.8526	21.7141
FQ634N	2	6349.20	43.00	4.69199e-18	22.2217	21.9002	21.7309
FQ672N	2	6716.40	69.98	1.50895e-17	20.9533	20.5097	20.2628
FQ674N	1	6730.70	39.21	2.16478e-17	20.5615	20.1133	19.8685
FQ727N	2	7275.20	63.22	5.13166e-18	22.1244	21.5072	21.1829
FQ750N	1	7502.50	28.12	4.97883e-18	22.1572	21.4732	21.1106
FQ889N	1	8892.10	55.51	5.58031e-18	22.0334	20.9805	20.4679
FQ906N	2	9057.80	57.32	5.62212e-18	22.0252	20.9322	20.4234
FQ924N	2	9247.60	46.29	6.70502e-18	21.8340	20.6959	20.1066
FQ937N	1	9372.40	54.81	7.43637e-18	21.7216	20.5544	20.0964

Table 12. UVIS Multiplicative factors for PHOTFLAM for selected aperture radii. We define r = 6 arcsec as the infinite aperture radius

pixel	**3**	**5**	**7**	**10**	**11**	**12**	**13**	**14**	**15**	**20**	**Inf**
arcsec	0.1189	0.1981	0.2773	0.3962	0.4358	0.4754	0.5151	0.5547	0.5943	0.7924	Inf.
F200LP	1.301	1.086	1.034	1.000	0.992	0.985	0.979	0.972	0.967	0.942	0.873
F218W	1.253	1.088	1.036	1.000	0.990	0.979	0.969	0.960	0.950	0.912	0.853
F225W	1.253	1.085	1.034	1.000	0.990	0.981	0.972	0.964	0.955	0.919	0.858
F275W	1.235	1.078	1.030	1.000	0.993	0.986	0.980	0.974	0.968	0.939	0.872
F280N	1.216	1.075	1.028	1.000	0.993	0.988	0.982	0.975	0.970	0.943	0.873
F300X	1.245	1.079	1.030	1.000	0.993	0.986	0.980	0.973	0.967	0.936	0.870
F336W	1.219	1.079	1.029	1.000	0.994	0.989	0.986	0.981	0.978	0.958	0.890
F343N	1.215	1.080	1.029	1.000	0.994	0.990	0.986	0.982	0.979	0.961	0.893
F350LP	1.246	1.083	1.034	1.000	0.992	0.987	0.983	0.978	0.975	0.962	0.903
F373N	1.198	1.078	1.029	1.000	0.996	0.990	0.986	0.983	0.980	0.966	0.900
F390M	1.204	1.079	1.031	1.000	0.994	0.989	0.985	0.981	0.978	0.963	0.897
F390W	1.215	1.079	1.030	1.000	0.993	0.989	0.985	0.981	0.978	0.965	0.899
F395N	1.210	1.081	1.031	1.000	0.996	0.991	0.987	0.983	0.980	0.966	0.899
F410M	1.208	1.080	1.032	1.000	0.993	0.989	0.985	0.981	0.978	0.966	0.901
F438W	1.214	1.081	1.032	1.000	0.995	0.989	0.985	0.982	0.978	0.967	0.906
F467M	1.204	1.083	1.036	1.000	0.993	0.989	0.985	0.981	0.977	0.967	0.910
F469N	1.213	1.085	1.037	1.000	0.993	0.988	0.984	0.981	0.977	0.965	0.906
F475W	1.217	1.081	1.034	1.000	0.995	0.989	0.985	0.981	0.977	0.966	0.908
F475X	1.230	1.081	1.033	1.000	0.995	0.989	0.985	0.981	0.977	0.966	0.908
F487N	1.204	1.081	1.035	1.000	0.995	0.989	0.985	0.982	0.978	0.967	0.910
F502N	1.200	1.079	1.034	1.000	0.993	0.988	0.984	0.981	0.977	0.966	0.912
F547M	1.224	1.083	1.036	1.000	0.993	0.987	0.983	0.979	0.975	0.964	0.911
F555W	1.223	1.082	1.035	1.000	0.993	0.988	0.984	0.980	0.976	0.965	0.911
F600LP	1.265	1.076	1.037	1.000	0.992	0.985	0.979	0.975	0.971	0.957	0.906
F606W	1.226	1.081	1.036	1.000	0.992	0.986	0.982	0.977	0.974	0.962	0.910
F621M	1.218	1.077	1.033	1.000	0.991	0.985	0.981	0.976	0.972	0.960	0.910
F625W	1.245	1.081	1.035	1.000	0.992	0.986	0.981	0.976	0.972	0.960	0.909
F631N	1.219	1.076	1.033	1.000	0.991	0.985	0.979	0.975	0.971	0.958	0.907
F645N	1.217	1.073	1.032	1.000	0.991	0.984	0.980	0.975	0.971	0.959	0.909
F656N	1.226	1.075	1.034	1.000	0.990	0.983	0.977	0.973	0.970	0.957	0.907
F657N	1.220	1.072	1.033	1.000	0.991	0.983	0.977	0.973	0.970	0.957	0.905
F658N	1.230	1.076	1.034	1.000	0.991	0.983	0.978	0.974	0.971	0.955	0.904
F665N	1.226	1.074	1.033	1.000	0.991	0.983	0.977	0.973	0.969	0.955	0.905
F673N	1.235	1.076	1.036	1.000	0.992	0.984	0.978	0.974	0.971	0.959	0.904
F680N	1.241	1.075	1.035	1.000	0.992	0.984	0.977	0.974	0.970	0.956	0.905
F689M	1.242	1.076	1.035	1.000	0.992	0.984	0.977	0.973	0.970	0.956	0.907
F763M	1.264	1.074	1.039	1.000	0.994	0.988	0.980	0.974	0.970	0.955	0.904
F775W	1.276	1.074	1.039	1.000	0.993	0.987	0.980	0.974	0.970	0.957	0.905
F814W	1.303	1.078	1.039	1.000	0.993	0.987	0.980	0.974	0.970	0.956	0.903
F845M	1.325	1.075	1.039	1.000	0.993	0.988	0.983	0.976	0.971	0.955	0.901
F850LP	1.392	1.091	1.043	1.000	0.990	0.983	0.978	0.972	0.966	0.948	0.888
F953N	1.440	1.103	1.048	1.000	0.987	0.979	0.974	0.968	0.964	0.945	0.887

Table 13. Encircled Energy Fractions for WFC3/UVIS Wide Filters

Aperture Radius		Encircled Energy Fractions: Wide Filters											
pixel	arcsec	F218W	F225W	F275W	F336W	F390W	F438W	F475W	F555W	F606W	F625W	F775W	F814W
3	0.1189	0.681	0.685	0.706	0.730	0.740	0.746	0.746	0.745	0.742	0.730	0.709	0.693
4	0.1585	0.746	0.753	0.770	0.790	0.799	0.806	0.809	0.812	0.813	0.810	0.807	0.795
5	0.1981	0.784	0.791	0.809	0.825	0.833	0.838	0.840	0.842	0.842	0.841	0.843	0.838
6	0.2377	0.807	0.814	0.832	0.850	0.856	0.861	0.862	0.864	0.861	0.861	0.858	0.856
7	0.2773	0.823	0.830	0.847	0.865	0.873	0.878	0.878	0.880	0.878	0.878	0.871	0.869
8	0.3170	0.834	0.841	0.857	0.876	0.885	0.891	0.891	0.893	0.891	0.891	0.885	0.882
9	0.3566	0.843	0.850	0.866	0.884	0.893	0.899	0.901	0.903	0.901	0.900	0.897	0.894
10	0.3962	0.853	0.858	0.872	0.890	0.899	0.906	0.908	0.911	0.910	0.909	0.905	0.903
11	0.4358	0.862	0.867	0.878	0.895	0.905	0.911	0.913	0.917	0.917	0.916	0.911	0.909
12	0.4754	0.871	0.875	0.884	0.900	0.909	0.916	0.918	0.922	0.923	0.922	0.917	0.915
13	0.5151	0.880	0.883	0.890	0.903	0.913	0.920	0.922	0.926	0.927	0.927	0.923	0.921
14	0.5547	0.889	0.890	0.895	0.907	0.916	0.923	0.926	0.930	0.931	0.931	0.929	0.927
15	0.5943	0.898	0.898	0.901	0.910	0.919	0.926	0.929	0.933	0.934	0.935	0.933	0.931
16	0.6339	0.906	0.906	0.907	0.914	0.921	0.929	0.931	0.936	0.937	0.938	0.936	0.934
17	0.6735	0.914	0.914	0.912	0.918	0.924	0.931	0.934	0.938	0.940	0.940	0.939	0.937
18	0.7132	0.922	0.921	0.918	0.922	0.927	0.933	0.936	0.940	0.942	0.943	0.942	0.940
19	0.7528	0.929	0.928	0.924	0.925	0.930	0.935	0.938	0.942	0.944	0.945	0.944	0.943
20	0.7924	0.935	0.934	0.929	0.929	0.932	0.937	0.940	0.944	0.946	0.947	0.946	0.945
21	0.8320	0.941	0.940	0.934	0.932	0.935	0.939	0.942	0.945	0.948	0.949	0.948	0.947
22	0.8716	0.946	0.945	0.939	0.936	0.938	0.942	0.944	0.947	0.949	0.950	0.950	0.949
23	0.9113	0.951	0.950	0.944	0.939	0.940	0.944	0.946	0.949	0.951	0.952	0.952	0.951
24	0.9509	0.956	0.955	0.948	0.942	0.943	0.946	0.948	0.950	0.952	0.953	0.953	0.952
25	0.9905	0.960	0.959	0.953	0.946	0.945	0.948	0.949	0.952	0.953	0.954	0.955	0.954
26	1.0301	0.963	0.962	0.956	0.949	0.948	0.950	0.951	0.953	0.955	0.956	0.956	0.955
27	1.0697	0.966	0.966	0.960	0.952	0.950	0.952	0.953	0.955	0.956	0.957	0.957	0.957
28	1.1094	0.969	0.968	0.963	0.955	0.953	0.954	0.955	0.956	0.957	0.958	0.958	0.958
29	1.1490	0.971	0.971	0.966	0.958	0.955	0.956	0.957	0.958	0.959	0.959	0.959	0.959
30	1.1886	0.974	0.973	0.969	0.961	0.957	0.958	0.958	0.959	0.960	0.961	0.960	0.960
31	1.2282	0.976	0.975	0.971	0.964	0.960	0.960	0.960	0.961	0.961	0.962	0.961	0.961
32	1.2678	0.978	0.977	0.973	0.966	0.962	0.961	0.962	0.962	0.963	0.963	0.962	0.962
33	1.3075	0.979	0.978	0.975	0.968	0.964	0.963	0.963	0.964	0.964	0.964	0.963	0.962
34	1.3471	0.981	0.980	0.977	0.971	0.966	0.965	0.965	0.965	0.965	0.965	0.964	0.963
35	1.3867	0.982	0.981	0.978	0.973	0.968	0.967	0.967	0.966	0.967	0.966	0.965	0.964
36	1.4263	0.984	0.983	0.981	0.975	0.970	0.969	0.968	0.968	0.968	0.968	0.966	0.965
37	1.4659	0.986	0.985	0.983	0.978	0.972	0.971	0.969	0.969	0.969	0.969	0.967	0.966
38	1.5056	0.988	0.987	0.986	0.980	0.974	0.972	0.971	0.970	0.970	0.970	0.968	0.967
39	1.5452	0.988	0.988	0.986	0.981	0.975	0.973	0.972	0.971	0.971	0.971	0.968	0.968
40	1.5848	0.989	0.988	0.987	0.982	0.976	0.975	0.973	0.972	0.972	0.971	0.969	0.969
45	1.7829	0.991	0.991	0.990	0.986	0.983	0.981	0.979	0.978	0.976	0.975	0.973	0.972
50	1.9810	0.993	0.993	0.992	0.991	0.989	0.987	0.985	0.983	0.980	0.979	0.976	0.976

Table 14. Encircled Energy Fractions for WFC3/UVIS Long Pass and Extremely Wide Filters

Aperture Radius		Encircled Energy Fractions: Long Pass and Extremely Wide Filters					
pixel	arcsec	F200LP	F350LP	F600LP	F850LP	F300X	F475X
3	0.1189	0.671	0.725	0.716	0.638	0.699	0.738
4	0.1585	0.761	0.799	0.806	0.753	0.767	0.807
5	0.1981	0.804	0.834	0.842	0.814	0.806	0.840
6	0.2377	0.829	0.857	0.859	0.837	0.829	0.862
7	0.2773	0.844	0.873	0.874	0.851	0.845	0.879
8	0.3170	0.856	0.886	0.887	0.863	0.855	0.891
9	0.3566	0.865	0.896	0.898	0.875	0.863	0.900
10	0.3962	0.873	0.903	0.906	0.888	0.870	0.908
11	0.4358	0.880	0.910	0.913	0.897	0.876	0.913
12	0.4754	0.886	0.915	0.920	0.903	0.882	0.918
13	0.5151	0.892	0.919	0.925	0.908	0.888	0.922
14	0.5547	0.898	0.923	0.929	0.914	0.894	0.926
15	0.5943	0.903	0.926	0.933	0.919	0.900	0.929
16	0.6339	0.908	0.929	0.936	0.925	0.906	0.931
17	0.6735	0.913	0.932	0.939	0.929	0.912	0.934
18	0.7132	0.918	0.934	0.942	0.932	0.918	0.936
19	0.7528	0.922	0.936	0.944	0.934	0.923	0.938
20	0.7924	0.927	0.939	0.947	0.937	0.929	0.940
21	0.8320	0.931	0.941	0.949	0.940	0.934	0.942
22	0.8716	0.935	0.943	0.950	0.943	0.939	0.944
23	0.9113	0.939	0.945	0.952	0.945	0.944	0.946
24	0.9509	0.942	0.947	0.953	0.947	0.948	0.948
25	0.9905	0.945	0.949	0.955	0.949	0.952	0.949
26	1.0301	0.948	0.951	0.956	0.951	0.956	0.951
27	1.0697	0.951	0.953	0.957	0.953	0.959	0.953
28	1.1094	0.954	0.955	0.958	0.955	0.962	0.955
29	1.1490	0.956	0.957	0.959	0.956	0.965	0.957
30	1.1886	0.958	0.958	0.960	0.958	0.968	0.958
31	1.2282	0.960	0.960	0.961	0.959	0.970	0.960
32	1.2678	0.962	0.962	0.962	0.960	0.972	0.962
33	1.3075	0.963	0.963	0.963	0.961	0.974	0.963
34	1.3471	0.965	0.965	0.964	0.962	0.976	0.965
35	1.3867	0.966	0.967	0.965	0.963	0.977	0.966
36	1.4263	0.968	0.968	0.966	0.965	0.980	0.968
37	1.4659	0.969	0.969	0.967	0.966	0.983	0.969
38	1.5056	0.971	0.970	0.968	0.967	0.985	0.970
39	1.5452	0.972	0.971	0.969	0.967	0.986	0.972
40	1.5848	0.973	0.972	0.970	0.968	0.986	0.973
45	1.7829	0.979	0.976	0.973	0.972	0.989	0.979
50	1.9810	0.985	0.980	0.976	0.975	0.992	0.985

Table 15. Encircled Energy Fractions for WFC3/UVIS Medium Filters

Aperture Radius		Encircled Energy Fractions: Medium Filters							
pixel	arcsec	F390M	F410M	F467M	F547M	F621M	F689M	F763M	F845M
3	0.1189	0.745	0.746	0.756	0.744	0.747	0.730	0.715	0.680
4	0.1585	0.798	0.802	0.811	0.812	0.819	0.813	0.811	0.791
5	0.1981	0.831	0.834	0.840	0.841	0.845	0.843	0.842	0.838
6	0.2377	0.853	0.856	0.862	0.863	0.863	0.860	0.857	0.855
7	0.2773	0.870	0.873	0.878	0.879	0.881	0.876	0.870	0.867
8	0.3170	0.882	0.886	0.892	0.891	0.893	0.890	0.884	0.879
9	0.3566	0.891	0.895	0.902	0.902	0.902	0.899	0.897	0.891
10	0.3962	0.897	0.901	0.910	0.911	0.910	0.907	0.904	0.901
11	0.4358	0.902	0.907	0.916	0.917	0.918	0.914	0.909	0.907
12	0.4754	0.907	0.911	0.920	0.923	0.924	0.922	0.915	0.912
13	0.5151	0.911	0.915	0.924	0.927	0.928	0.928	0.922	0.917
14	0.5547	0.914	0.918	0.928	0.931	0.932	0.932	0.928	0.923
15	0.5943	0.917	0.921	0.931	0.934	0.936	0.935	0.932	0.928
16	0.6339	0.919	0.924	0.933	0.937	0.939	0.939	0.935	0.932
17	0.6735	0.922	0.926	0.936	0.939	0.942	0.942	0.938	0.935
18	0.7132	0.925	0.928	0.938	0.942	0.944	0.944	0.942	0.937
19	0.7528	0.928	0.930	0.939	0.943	0.946	0.946	0.944	0.940
20	0.7924	0.931	0.933	0.941	0.945	0.948	0.949	0.947	0.943
21	0.8320	0.934	0.935	0.943	0.947	0.949	0.951	0.949	0.946
22	0.8716	0.937	0.937	0.945	0.948	0.951	0.953	0.951	0.947
23	0.9113	0.939	0.939	0.947	0.949	0.953	0.954	0.953	0.948
24	0.9509	0.942	0.942	0.949	0.951	0.954	0.955	0.955	0.950
25	0.9905	0.945	0.944	0.950	0.952	0.955	0.956	0.956	0.951
26	1.0301	0.948	0.947	0.952	0.953	0.957	0.957	0.957	0.953
27	1.0697	0.950	0.949	0.954	0.955	0.958	0.958	0.958	0.954
28	1.1094	0.952	0.951	0.956	0.956	0.959	0.959	0.959	0.955
29	1.1490	0.955	0.953	0.957	0.958	0.960	0.960	0.959	0.957
30	1.1886	0.957	0.955	0.959	0.959	0.961	0.961	0.960	0.958
31	1.2282	0.959	0.957	0.961	0.960	0.962	0.962	0.960	0.959
32	1.2678	0.961	0.960	0.962	0.962	0.963	0.963	0.961	0.961
33	1.3075	0.964	0.962	0.964	0.963	0.964	0.964	0.962	0.962
34	1.3471	0.966	0.965	0.965	0.965	0.965	0.965	0.963	0.963
35	1.3867	0.968	0.967	0.967	0.966	0.966	0.966	0.965	0.964
36	1.4263	0.970	0.969	0.968	0.968	0.968	0.967	0.966	0.965
37	1.4659	0.972	0.971	0.970	0.969	0.969	0.968	0.967	0.966
38	1.5056	0.974	0.973	0.971	0.970	0.970	0.969	0.968	0.967
39	1.5452	0.976	0.974	0.972	0.971	0.971	0.970	0.969	0.967
40	1.5848	0.977	0.975	0.974	0.972	0.971	0.971	0.969	0.968
45	1.7829	0.983	0.982	0.980	0.977	0.975	0.974	0.973	0.972
50	1.9810	0.989	0.988	0.986	0.982	0.979	0.977	0.976	0.975

Table 16. Encircled Energy Fractions for WFC3/UVIS Narrow Band Filters, UV – VIS.

Aperture Radius		Encircled Energy Fractions: Narrow Band Filters							
pixel	arcsec	F280N	F343N	F373N	F395N	F469N	F487N	F502N	F631N
3	0.1189	0.718	0.735	0.751	0.743	0.747	0.756	0.760	0.744
4	0.1585	0.776	0.793	0.803	0.799	0.805	0.813	0.817	0.817
5	0.1981	0.812	0.827	0.835	0.832	0.835	0.842	0.845	0.843
6	0.2377	0.835	0.851	0.858	0.854	0.857	0.863	0.866	0.861
7	0.2773	0.849	0.868	0.875	0.872	0.874	0.879	0.882	0.878
8	0.3170	0.859	0.879	0.886	0.884	0.888	0.892	0.894	0.891
9	0.3566	0.867	0.887	0.894	0.892	0.898	0.902	0.905	0.899
10	0.3962	0.873	0.893	0.900	0.899	0.906	0.910	0.912	0.907
11	0.4358	0.879	0.898	0.904	0.903	0.912	0.915	0.918	0.915
12	0.4754	0.884	0.902	0.909	0.907	0.917	0.920	0.923	0.921
13	0.5151	0.889	0.906	0.913	0.911	0.921	0.924	0.927	0.926
14	0.5547	0.895	0.909	0.916	0.915	0.924	0.927	0.930	0.930
15	0.5943	0.900	0.912	0.918	0.917	0.927	0.930	0.933	0.934
16	0.6339	0.905	0.915	0.920	0.920	0.930	0.933	0.936	0.937
17	0.6735	0.910	0.919	0.923	0.922	0.932	0.936	0.939	0.940
18	0.7132	0.916	0.923	0.926	0.925	0.935	0.938	0.941	0.942
19	0.7528	0.921	0.926	0.929	0.928	0.937	0.940	0.943	0.944
20	0.7924	0.926	0.929	0.932	0.931	0.939	0.941	0.944	0.947
21	0.8320	0.931	0.933	0.934	0.933	0.941	0.943	0.945	0.949
22	0.8716	0.936	0.936	0.936	0.936	0.943	0.944	0.947	0.951
23	0.9113	0.941	0.939	0.939	0.938	0.945	0.946	0.948	0.953
24	0.9509	0.946	0.942	0.942	0.941	0.947	0.948	0.949	0.954
25	0.9905	0.950	0.945	0.945	0.943	0.949	0.949	0.951	0.955
26	1.0301	0.954	0.948	0.949	0.946	0.951	0.951	0.952	0.956
27	1.0697	0.958	0.951	0.952	0.948	0.953	0.953	0.953	0.958
28	1.1094	0.962	0.954	0.956	0.950	0.955	0.955	0.955	0.959
29	1.1490	0.965	0.957	0.958	0.953	0.957	0.957	0.956	0.960
30	1.1886	0.967	0.960	0.959	0.955	0.958	0.959	0.959	0.961
31	1.2282	0.970	0.963	0.962	0.958	0.960	0.960	0.961	0.963
32	1.2678	0.972	0.965	0.964	0.960	0.962	0.962	0.962	0.963
33	1.3075	0.974	0.968	0.966	0.963	0.963	0.964	0.964	0.964
34	1.3471	0.976	0.970	0.968	0.965	0.965	0.965	0.965	0.965
35	1.3867	0.977	0.972	0.970	0.968	0.967	0.967	0.966	0.966
36	1.4263	0.980	0.974	0.972	0.970	0.968	0.968	0.968	0.968
37	1.4659	0.982	0.977	0.974	0.972	0.970	0.969	0.969	0.969
38	1.5056	0.985	0.979	0.976	0.974	0.971	0.971	0.970	0.970
39	1.5452	0.986	0.980	0.977	0.975	0.972	0.972	0.971	0.971
40	1.5848	0.986	0.981	0.978	0.976	0.974	0.973	0.973	0.971
45	1.7829	0.989	0.986	0.984	0.982	0.980	0.979	0.978	0.975
50	1.9810	0.992	0.990	0.989	0.989	0.986	0.985	0.984	0.979

Table 17. Encircled Energy Fractions for WFC3/UVIS Narrow Band Filters, VIS-NIR

Aperture Radius		Encircled Energy Fractions: Narrow Band Filters							
pixel	arcsec	F645N	F656N	F657N	F658N	F665N	F673N	F680N	F953N
3	0.1189	0.747	0.740	0.742	0.735	0.738	0.732	0.729	0.616
4	0.1585	0.821	0.817	0.818	0.813	0.817	0.814	0.814	0.733
5	0.1981	0.847	0.844	0.844	0.840	0.843	0.840	0.842	0.804
6	0.2377	0.865	0.860	0.860	0.857	0.859	0.856	0.858	0.831
7	0.2773	0.881	0.877	0.876	0.874	0.876	0.873	0.874	0.846
8	0.3170	0.894	0.891	0.889	0.888	0.889	0.887	0.889	0.861
9	0.3566	0.902	0.900	0.898	0.897	0.898	0.897	0.898	0.873
10	0.3962	0.909	0.907	0.905	0.904	0.905	0.904	0.905	0.887
11	0.4358	0.917	0.916	0.913	0.912	0.913	0.911	0.912	0.899
12	0.4754	0.924	0.923	0.921	0.920	0.921	0.919	0.920	0.906
13	0.5151	0.928	0.928	0.926	0.924	0.926	0.924	0.926	0.911
14	0.5547	0.932	0.932	0.930	0.928	0.930	0.928	0.929	0.916
15	0.5943	0.936	0.935	0.933	0.931	0.934	0.931	0.933	0.920
16	0.6339	0.939	0.939	0.937	0.935	0.938	0.934	0.937	0.926
17	0.6735	0.941	0.942	0.939	0.939	0.941	0.938	0.940	0.932
18	0.7132	0.943	0.944	0.942	0.941	0.943	0.940	0.943	0.935
19	0.7528	0.945	0.946	0.944	0.944	0.945	0.941	0.944	0.937
20	0.7924	0.948	0.948	0.946	0.947	0.948	0.943	0.947	0.939
21	0.8320	0.949	0.950	0.949	0.949	0.950	0.946	0.949	0.942
22	0.8716	0.951	0.952	0.950	0.950	0.951	0.948	0.951	0.945
23	0.9113	0.953	0.954	0.951	0.951	0.953	0.949	0.953	0.948
24	0.9509	0.954	0.955	0.953	0.953	0.954	0.951	0.953	0.950
25	0.9905	0.955	0.957	0.955	0.955	0.955	0.953	0.954	0.951
26	1.0301	0.956	0.958	0.955	0.957	0.957	0.955	0.956	0.952
27	1.0697	0.957	0.960	0.956	0.958	0.958	0.957	0.956	0.953
28	1.1094	0.958	0.961	0.957	0.960	0.959	0.958	0.957	0.956
29	1.1490	0.960	0.962	0.959	0.961	0.960	0.959	0.958	0.958
30	1.1886	0.961	0.963	0.961	0.962	0.960	0.961	0.960	0.960
31	1.2282	0.961	0.963	0.962	0.964	0.961	0.962	0.961	0.961
32	1.2678	0.962	0.963	0.962	0.965	0.962	0.963	0.962	0.962
33	1.3075	0.964	0.964	0.964	0.965	0.963	0.964	0.963	0.963
34	1.3471	0.965	0.965	0.965	0.966	0.965	0.965	0.964	0.964
35	1.3867	0.966	0.966	0.966	0.966	0.966	0.966	0.966	0.965
36	1.4263	0.967	0.967	0.967	0.967	0.967	0.967	0.967	0.966
37	1.4659	0.969	0.968	0.968	0.968	0.968	0.968	0.968	0.967
38	1.5056	0.970	0.970	0.970	0.970	0.969	0.969	0.969	0.968
39	1.5452	0.970	0.970	0.970	0.970	0.970	0.970	0.970	0.969
40	1.5848	0.971	0.971	0.971	0.971	0.971	0.971	0.971	0.970
45	1.7829	0.975	0.974	0.974	0.974	0.974	0.974	0.974	0.973
50	1.9810	0.978	0.978	0.978	0.978	0.978	0.977	0.977	0.976

Values for encircled energy fractions between 0.1 and 2.0 arcsec from Hartig's (2009) revised encircled energy model are included for convenience in Table 18. These EE values are determined from high signal to noise observations of a bright star, and measured at aperture radii between 0.1 and 6 arcsec.

Table 18. Model WFC3/UVIS PSF Encircled Energy Fraction vs. Aperture Radius

Radius	Wavelength (μm)									
arcsec	0.2	0.3	0.4	0.5	0.6	0.7	0.8	0.9	1	1.1
0.1	0.660	0.739	0.754	0.745	0.720	0.687	0.650	0.623	0.612	0.605
0.15	0.717	0.793	0.823	0.834	0.832	0.823	0.807	0.778	0.742	0.699
0.2	0.752	0.822	0.845	0.859	0.859	0.857	0.853	0.847	0.844	0.829
0.25	0.781	0.844	0.864	0.875	0.877	0.874	0.87	0.867	0.868	0.864
0.3	0.802	0.858	0.880	0.888	0.890	0.889	0.883	0.879	0.879	0.876
0.4	0.831	0.880	0.899	0.911	0.910	0.907	0.906	0.904	0.900	0.894
0.5	0.861	0.894	0.912	0.923	0.925	0.923	0.918	0.915	0.918	0.917
0.6	0.884	0.906	0.922	0.932	0.934	0.933	0.931	0.927	0.927	0.923
0.8	0.936	0.928	0.936	0.944	0.947	0.946	0.945	0.942	0.944	0.942
1.0	0.967	0.946	0.948	0.954	0.955	0.955	0.955	0.952	0.955	0.952
1.5	0.989	0.984	0.973	0.970	0.970	0.969	0.967	0.966	0.97	0.968
2.0	0.994	0.992	0.989	0.985	0.980	0.977	0.976	0.975	0.978	0.976

Table 19. PSF Data for F275W and F625W from Program as measured by G. Hartig (2009). At large apertures the differences with spatial position is negligible, at 0.5 arcsec, the difference is 0.1%, but at small radii, effects of spatial variation are of order 1%.

	Position (pixel)		Aperture Diameter (arcsec and pixels)						
filt_pos	x	y	0.2	0.25	0.5	1	2	4	6
			5.05	6.31	12.62	25.24	50.48	100.96	151.44
F275W_a	741.1	3264.9	0.687	0.736	0.839	0.882	0.948	0.985	0.992
F275W_b	3296.8	3282.9	0.710	0.760	0.843	0.885	0.949	0.985	0.993
F275W_c	743	701.2	0.699	0.753	0.841	0.884	0.949	0.985	0.993
F275W_d	3277.8	735.8	0.705	0.763	0.843	0.886	0.950	0.985	0.993
F275W_m	2007.1	2282	0.706	0.753	0.841	0.882	0.948	0.986	0.994
F625W_a	728	3278.7	0.71	0.786	0.868	0.923	0.951	0.978	0.992
F625W_b	3284	3271.1	0.715	0.784	0.875	0.924	0.953	0.979	0.993
F625W_c	755.1	713.1	0.713	0.784	0.873	0.924	0.952	0.978	0.992
F625W_d	3290.1	722.1	0.731	0.796	0.883	0.927	0.955	0.979	0.993
F625W_m	1994.3	2270.2	0.705	0.784	0.873	0.922	0.952	0.978	0.993

Appendix B: Sample Aperture Photometry

Listed in Table 20 are aperture photometry performed on FLT files for GD153 images processed with the updated calwf3, using the chip dependent reference files, and obtained from the MAST. Aperture photometry used the PyRAF task *daophot*. WFC3 UVIS FLT files are in units of electrons. To obtain the count rate, divide the aperture signal by the exposure time. These FLT files do not have cosmic ray or hot pixel flagging.

Table 20. Sample Aperture Photometry For Three FLT Files

dataset		**ibnx14w0q**	**ibcd05l8q**	**ibwi03brq**
CCD		UVIS2 – AMP C	UVIS1- AMP A	UVIS2- AMP C
X center		285.106	201.248	261.218
Y center		201.309	291.547	260.057
Filter		F336W	F438W	F814W
Exptime (sec)		5.5	6	15
		FLT Flux (electrons)		
aperture radius in pixels	3	302088.8	265687.8	279302.1
	5	329548.5	293835.1	329031.6
	10	347749.5	317962.4	351791.4
	15	353004.5	324557.1	357986.3
	20	357145.2	327235.7	360594.5
		FLT*PAM Flux (electrons)		
aperture radius in pixels	3	293131.6	257416.4	279276.8
	5	319777.2	284687.2	329001.8
	10	337438.3	308063.3	351759.5
	15	342537.3	314452.9	357954.0
	20	346554.8	317048.4	360561.8

DAOPHOT Parameters are:

-> lpar fitskypars

```
 (salgorithm = "mean")    Sky fitting algorithm
    (annulus = 152.0)     Inner radius of sky annulus in scale units
  (dannulus = 45.0)       Width of sky annulus in scale units
  (skyvalue = 0.0)        User sky value
  (smaxiter = 10)         Maximum number of sky fitting iterations
   (sloclip = 0.0)        Lower clipping factor in percent
   (shiclip = 0.0)        Upper clipping factor in percent
  (snreject = 50)         Maximum number of sky fitting rejection iterations
 (sloreject = 3.0)        Lower K-sigma rejection limit in sky sigma
 (shireject = 3.0)        Upper K-sigma rejection limit in sky sigma
     (khist = 3.0)        Half width of histogram in sky sigma
  (binsize = 0.1)         Binsize of histogram in sky sigma
   (smooth = no)          Boxcar smooth the histogram
    (rgrow = 0.0)         Region growing radius in scale units
    (mksky = no)          Mark sky annuli on the display
     (mode = "al")
```

->lpar findpars

```
  (threshold = 12.0)   Threshold in sigma for feature detection
      (nsigma = 1.5)   Width of convolution kernel in sigma
       (ratio = 1.0)   Ratio of minor to major axis of Gaussian kernel
       (theta = 0.0)   Position angle of major axis of Gaussian kernel
     (sharplo = 0.5)   Lower bound on sharpness for feature detection
     (sharphi = 0.8)   Upper bound on sharpness for feature detection
     (roundlo = -0.3)  Lower bound on roundness for feature detection
     (roundhi = 0.5)   Upper bound on roundness for feature detection
(mkdetections = no)    Mark detections on the image display?
        (mode = "ql")
```

Appendix C: Reprocessing WFC3/UVIS data

CALWF3 version 3.3 was ingested into OPUS on February 23, 2016. The CALWF3 pipeline now provides chip-dependent photometry and CTE correction. Users who want to compare current observation to data obtained prior to this date can re-retrieve their images from MAST. For those who wish to reprocess pre-2016 data themselves, we describe the steps here, however, users should consult the Reference Guide (Ryan et al. 2016) and the Cookbook (Bajaj 2016) for more information.

Processing Steps:

1. Update the new science software via AstroConda at http://astroconda.readthedocs.io
2. Request Datasets
    a. Retrieve from MAST the uncalibrated data (*_raw.fits) and select best reference files. Alternatively, obtain the bias and dark files, and, the bad pixel (BPIXTAB), detector characteristics (CCDTAB), overscan region (OSCNTAB), cosmic ray rejection (CRREJTAB), multidrizzle (MDRIZTAB) and pixel area correction (PAM) tables from http://www.stsci.edu/hst/observatory/crds.
    b. Obtain the chip-dependent flats from https://hst-crds.stsci.edu/. To access the files, click on the link for 'wfc3', 'pfltfile', and select the appropriate filter flat with 'Activation Date=Feb 23, 2016'. The new flats are named 'zcv205*pfl.fits'.
3. Edit and/or add header keywords to the 0th extension of the science data using a fits header editor. The two keywords, FLUXCORR and PHOTCORR, will need to be added, and set to PERFORM, the PFLTFILE and IMPHTTAB keyword values will need to be changed to the new flatfield file and new imphttab file. By default, WFC3 calibration reference files are assumed to be in a directory called *iref,* and the keyword value will include it, e.g. for BPIXTAB = iref$my_bpx.fits. /". If the reference files are in a different directory remember to include the directory path, e.g. 'refdirectory/my_bpx.fits', though if the path is too long an alternative is to set the path in the login.cl file, for example,

set iref="/user/reference/directory/".

Example of edited header keywords.

/ CALIBRATION REFERENCE FILES

```
BPIXTAB = 'my_bpx.fits' / bad pixel table
CCDTAB = 'my_ccd.fits' / detector calibration parameters
ATODTAB = 'my_a2d.fits' / analog to digital correction file
OSCNTAB = 'my_osc.fits' / detector overscan table
BIASFILE= 'my_bia.fits' / bias image file name
FLSHFILE= 'N/A ' / post flash correction file name
CRREJTAB= 'my_crr.fits' / cosmic ray rejection parameters
SHADFILE= 'N/A ' / shutter shading correction file
DARKFILE= 'my_drk.fits' / dark image file name
PFLTFILE= 'my_two_chip_pfl.fits'    / pixel to pixel flat field file
DFLTFILE= 'N/A ' / delta flat field file name
```

```
LFLTFILE= 'N/A ' / low order flat
GRAPHTAB= 'my_tmg.fits' / the HST graph table
COMPTAB = my_tmc.fits_'/ the HST components table
IMPHTTAB= 'new_imp.fits'/ Image Photometry Table
IDCTAB = 'my_idc.fits' / image distortion correction table
DGEOFILE= 'N/A ' / Distortion correction image
MDRIZTAB= 'my_mdz.fits' / MultiDrizzle parameter table
D2IMFILE= 'my_d2i.fits' / Column Correction Reference File
FLUXCORR = 'PERFORM' /
PHOTCORR = 'PERFORM' /
```

4. Run CALWF3. Examples of how to run the code (Sosey & Hack, WFC3 STAN Jan 2013)

   a. In Python, without Teal:

   ```
   >>> from wfc3tools import calwf3
   >>> calwf3.calwf3(filename)
   ```

   b. In Python, with Teal:

   ```
   >>> from stsci.tools import teal
   >>> from wfc3tools import calwf3
   >>> teal.teal('calwf3')
   ```

   c. In PyRAF:

   ```
   >>> import wfc3tools
   >>> epar calwf3
   ```

   d. From the command line:

   ```
   > calwf3.e filename
   ```

5. CTE Corrections. Once calwf3 has processed the raw data (*_raw.fits) the resulting files will have been renamed to *_flt.fits. Users, who wish to apply CTE corrections, should do so now. Software tools and instructions are available at http://www.stsci.edu/hst/wfc3/ins_performance/CTE/

6. Astrodrizzle**.** At this point users have the option of using AstroDrizzle to correct for distortion and combine datasets. Instructions on how to use Astrodrizzle may be found at http://www.stsci.edu/hst/HST_overview/drizzlepac. .

For users who prefer to work with calibrated *flt.fits, *flc.fits data products, the geometric distortion model is unchanged in the chip-dependent model, so the same set of pixel area map corrections (PAMs) may be used (http://www.stsci.edu/hst/wfc3/pam/pixel_area_maps).